npj | Quantum Information

www.nature.com/npjqi

ARTICLE OPEN

Proposal to test quantum wave-particle superposition on massive mechanical resonators

Wei Qin[1,2], Adam Miranowicz[1,3], Guilu Long[4,5,6], J. Q. You[2,7] and Franco Nori[1,8]

We present and analyze a proposal for a macroscopic quantum delayed-choice experiment with massive mechanical resonators. In our approach, the electronic spin of a single nitrogen-vacancy impurity is employed to control the coherent coupling between the mechanical modes of two carbon nanotubes. We demonstrate that a mechanical phonon can be in a coherent superposition of wave and particle, thus exhibiting both behaviors at the same time. We also discuss the mechanical noise tolerable in our proposal and predict a critical temperature below which the morphing between wave and particle states can be effectively observed in the presence of environment-induced fluctuations. Furthermore, we describe how to amplify single-phonon excitations of the mechanical-resonator superposition states to a macroscopic level, via squeezing the mechanical modes. This approach corresponds to the phase-covariant cloning. Therefore, our proposal can serve as a test of macroscopic quantum superpositions of massive objects even with large excitations. This work, which describes a fundamental test of the limits of quantum mechanics at the macroscopic scale, would have implications for quantum metrology and quantum information processing.

npj Quantum Information (2019)5:58 ; https://doi.org/10.1038/s41534-019-0172-9

INTRODUCTION

Wave-particle duality lies at the heart of quantum physics. According to Bohr's complementarity principle,[1] a quantum system may behave either as a wave or as a particle depending on the measurement apparatus, and both behaviors are never observed simultaneously. This can be well demonstrated via a single photon Mach–Zehnder interferometer, as depicted in Fig. 1a. An incident photon is split, at an input beam-splitter BS_1, into an equal superposition of being in the upper and lower paths. This is followed by a phase shift ϕ in the upper path. At the output beam-splitter BS_2, the paths are recombined and the detection probability in the detector D_1 or D_2 depends on the phase ϕ, heralding the wave nature of a single photon. If, however, BS_2 is absent, the photon is detected with probability 1/2 in each detector, and thus, shows its particle nature. In Wheeler's delayed-choice experiment,[2,3] the decision of whether or not to insert BS_2 is randomly made after a photon is already inside the interferometer. The arrangement rules out a hidden-variable theory, which suggests that the photon may determine, in advance, which behavior, wave or particle, to exhibit through a hidden variable.[4–11] Recently, a quantum delayed-choice experiment, where BS_2 is engineered to be in a quantum superposition of being present and absent, has been proposed.[12] Such a version allows a single system to be in a quantum superposition of a wave and a particle, so that both behaviors can be observed in a single measurement apparatus at the same time.[13,14] This extends the conventional boundary of Bohr's complementarity principle. The quantum delayed-choice experiment has already been implemented in nuclear magnetic resonance,[15–17] optics,[18–23] and superconducting circuits.[24,25] However, all these experiments were performed essentially at the microscopic scale.

Here, as a step in the macroscopic test for a coherent wave-particle superposition on massive objects, we propose and analyze an approach for a mechanical quantum delayed-choice experiment. Mechanical systems are not only being explored now for potential quantum technologies,[26,27] but they also have been considered as a promising candidate to test fundamental principles in quantum theory.[28] In this manuscript, we demonstrate that, similar to a single photon, the mechanical phonon can be prepared in a quantum superposition of both a wave and a particle. The basic idea is to use a single nitrogen-vacancy (NV) center in diamond to control the coherent coupling between two separated carbon nanotubes (CNTs).[29,30] We focus on the electronic ground state of the NV center, which is a spin $S = 1$ triplet with a zero-field splitting $D \simeq 2\pi \times 2.87$ GHz between spin states $|0\rangle$ and $|\pm 1\rangle$ [see Fig. 1b]. If the spin is in $|0\rangle$, the mechanical modes are decoupled, and otherwise are coupled. Moreover, the mechanical noise tolerated by our proposal is evaluated and we show a critical temperature, below which the coherent signal is resolved.

RESULTS

Physical model

We consider a hybrid system[31,32] consisting of two (labelled as $k = 1, 2$) parallel CNTs and an NV electronic spin, as illustrated in Fig. 1c. The CNTs, both suspended along the $\hat{x}$-direction, carry dc currents I_1 and I_2, respectively, while the spin is placed between

[1]Theoretical Quantum Physics Laboratory, RIKEN Cluster for Pioneering Research, Wako-shi, Saitama 351-0198, Japan; [2]Quantum Physics and Quantum Information Division, Beijing Computational Science Research Center, 100193 Beijing, China; [3]Faculty of Physics, Adam Mickiewicz University, 61-614 Poznań, Poland; [4]State Key Laboratory of Low-Dimensional Quantum Physics and Department of Physics, Tsinghua University, 100084 Beijing, China; [5]Beijing Academy of Quantum Information Science, 100193 Beijing, China; [6]Beijing National Research Center for Information Science and Technology, 100084 Beijing, China; [7]Department of Physics and State Key Laboratory of Modern Optical Instrumentation, Zhejiang University, 310027 Hangzhou, China and [8]Department of Physics, The University of Michigan, Ann Arbor, MI 48109-1040, USA
Correspondence: J. Q. You (jqyou@zju.edu.cn) or Franco Nori (fnori@riken.jp)

Received: 20 December 2018 Accepted: 17 June 2019
Published online: 09 July 2019

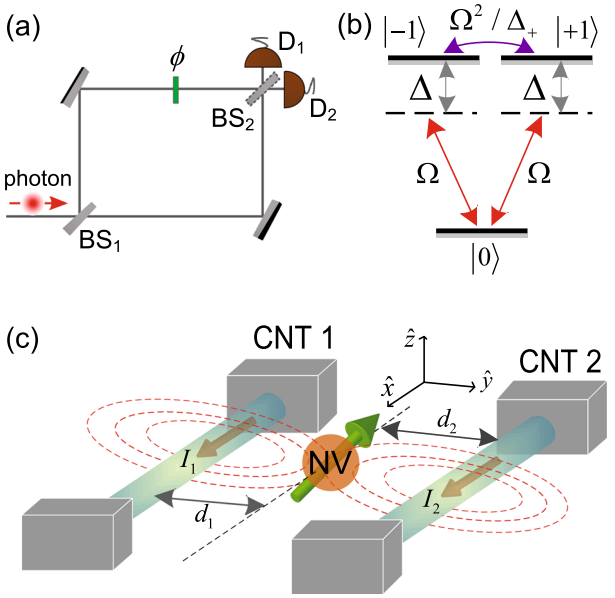

Fig. 1 **a** Demonstration of the wave-particle duality using a Mach–Zehnder interferometer. A single photon is first split at the input beam-splitter BS_1, then undergoes a phase shift ϕ and finally is observed at detectors D_1 and D_2. The photon behaves as a wave if the output beam-splitter BS_2 is inserted, or as a particle if BS_2 is removed. In quantum delayed-choice experiments, BS_2 is set in a quantum superposition of being present and absent, and consequently, the photon can simultaneously exhibit its wave and particle nature. **b** Level structure of the driven NV spin in the electronic ground state. Here we have assumed that the Zeeman splitting between the spin states $|\pm1\rangle$ is eliminated by applying an external field. **c** Schematic representation of a mechanical quantum delayed-choice experiment with an NV electronic spin and two CNTs. The mechanical vibrations of the CNTs are completely decoupled or coherently coupled, depending, respectively, on whether or not the intermediate spin is in the spin state $|0\rangle$, with the dc current I_k through the kth CNT, and the distance d_k between the spin and the kth CNT

them, at a distance d_1 from the first CNT and at a distance d_2 from the second CNT. When vibrating along the $\hat{y}$-direction, the CNTs can parametrically modulate the Zeeman splitting of the intermediate spin through the magnetic field, yielding a magnetic coupling to the spin.[33–37] For simplicity, below we assume that the CNTs are identical such that they have the same vibrational frequency ω_m and the same vibrational mass m. The mechanical vibrations are modelled by quantized harmonic oscillators with a Hamiltonian

$$H_{\rm mv} = \sum_{k=1,2} \hbar\omega_m b_k^\dagger b_k, \tag{1}$$

where b_k ($b_k^\dagger$) denotes the phonon annihilation (creation) operator. The Hamiltonian characterizing the coupling of the mechanical modes to the spin is

$$H_{\rm int} = \sum_{k=1,2} \hbar g_k S_z q_k, \tag{2}$$

where $S_z = |+1\rangle\langle+1| - |-1\rangle\langle-1|$ is the z-component of the spin, $q_k = b_k + b_k^\dagger$ represents the canonical phonon position operator, and $g_k = \mu_B g_s y_{\rm zp} G_k/\hbar$ refers to the Zeeman shift corresponding to the zero-point motion $y_{\rm zp} = [\hbar/(2m\omega_m)]^{1/2}$. Here, μ_B is the Bohr magneton, $g_s \simeq 2$ is the Landé factor, and $G_k = \mu_0 I_k/(2\pi d_k^2)$ is the magnetic-field gradient, where μ_0 is the vacuum permeability. In order to mediate the coherent coupling of the CNT mechanical modes through the spin, we apply a time-dependent magnetic field

$$B_x(t) = B_0 \cos(\omega_0 t), \tag{3}$$

with amplitude B_0 and frequency ω_0, along the $\hat{x}$-direction, to drive the $|0\rangle \to |\pm1\rangle$ transitions with Rabi frequency

$$\Omega = \frac{\mu_B g_s B_0}{2\sqrt{2}\hbar}. \tag{4}$$

We apply a static magnetic field

$$B_z = \sum_{k=1,2} (-1)^k d_k G_k, \tag{5}$$

along the $\hat{z}$-direction to eliminate the Zeeman splitting between the spin states $|\pm1\rangle$.[36] This causes the same Zeeman shift,

$$\Delta = \Delta_- + \frac{3\Omega^2}{\Delta_+}, \tag{6}$$

where $\Delta_\pm = D \pm \omega_0$, to be imprinted on $|\pm1\rangle$, and a coherent coupling, of strength Ω^2/Δ_+, between them, as shown in Fig. 1b. We can, thus, introduce a dark state

$$|D\rangle = (|+1\rangle - |-1\rangle)/\sqrt{2}, \tag{7}$$

and a bright state

$$|B\rangle = (|+1\rangle + |-1\rangle)/\sqrt{2}, \tag{8}$$

with an energy splitting $\simeq 2\Omega^2/\Delta_+$. In this case, the spin state $|0\rangle$ is decoupled from the dark state, and is dressed by the bright state. Under the assumption of $\Omega/\Delta \ll 1$, the dressing will only increase the energy splitting between the dark and bright states to

$$\omega_q \simeq 2\Omega^2\left(\frac{1}{\Delta} + \frac{1}{\Delta_+}\right). \tag{9}$$

This yields a spin qubit with $|D\rangle$ as the ground state and $|B\rangle$ as the exited state. The spin-CNT coupling Hamiltonian is accordingly transformed to

$$H_{\rm int} \simeq \sum_{k=1,2} \hbar g_k \sigma_x q_k, \tag{10}$$

where $\sigma_x = \sigma_+ + \sigma_-$, with $\sigma_- = |D\rangle\langle B|$ and $\sigma_+ = \sigma_-^\dagger$. When we further restrict our discussion to a dispersive regime $\omega_q \pm \omega_m \gg |g_k|$, the spin qubit becomes a quantum data bus, allowing for mechanical excitations to be exchanged between the CNTs. By using a time-averaging treatment,[38,39] the unitary dynamics of the system is then described by an effective Hamiltonian (see Supplementary Section 1 for a detailed derivation), $H_{\rm eff} = H_{\rm cnt} \otimes \sigma_z$, where

$$H_{\rm cnt} = \frac{2\hbar\omega_q}{\omega_q^2 - \omega_m^2}\left[\sum_{k=1,2} g_k^2 b_k^\dagger b_k + g_1 g_2\left(b_1 b_2^\dagger + {\rm H.c.}\right)\right], \tag{11}$$

and $\sigma_z = |B\rangle\langle B| - |D\rangle\langle D|$. The Hamiltonian $H_{\rm cnt}$ includes a coherent spin-mediated CNT–CNT coupling in the beam-splitter form, which is conditioned on the spin state. Here, we neglect the direct CNT–CNT coupling much smaller than the spin-mediated coupling, as is described in Supplementary Section 1. Furthermore, we find that the decoupling of one CNT from the spin gives rise to a spin-induced shift of the vibrational resonance of the other CNT. Hence, the dynamics described by $H_{\rm eff}$ can be used to implement controlled Hadamard and phase gates.

Quantum delayed-choice experiment with mechanical resonators

Let us first discuss the Hadamard gate. Having $I_k = I$ and $d_k = d$ gives a symmetric coupling $g_k = g$, and a mechanical beam-splitter coupling of strength

$$J = \frac{2g^2\omega_q}{\omega_q^2 - \omega_m^2}. \tag{12}$$

Unitary evolution for a time $\tau_0 = \pi/(4J)$ then leads to

$$b_1(\tau_0) = (b_1 - ib_2)/\sqrt{2}, \tag{13}$$

$$b_2(\tau_0) = (b_2 - ib_1)/\sqrt{2}. \tag{14}$$

For the phase gate, we can turn off the current, for example, of the second CNT, so that $g_1 = g$ and $g_2 = 0$. In this case, a dispersive shift of $\simeq J$ is imprinted into the vibrational resonance of the first CNT, which in turn introduces a relative phase $\phi \simeq J\tau_1$ after a time τ_1 under unitary evolution. Note that, here, both Hadamard and phase gates are controlled operations conditional on the spin state, as mentioned before. The two gates and their timing errors are analyzed in detail in the Supplementary Section 2.

We now turn to the quantum delayed-choice experiment with the macroscopic CNTs. We assume that the hybrid system is initially prepared in the state

$$|\Psi\rangle_i = \left(b_1^\dagger \otimes \mathcal{I}_2|\mathrm{vac}\rangle\right) \otimes |D\rangle, \tag{15}$$

where $|\mathrm{vac}\rangle$ refers to the phonon vacuum and $\mathcal{I}_k$ is the identity operator for the kth CNT. After the initialization, the currents are tuned to be $I_k = I$, to drive the system for a time τ_0, and the resulting Hadamard operation splits the single phonon into an equal superposition across both CNTs. Then, we turn off I_2 for a time τ_1 to accumulate a relative phase between the CNTs. While achieving the desired phase ϕ, we turn on I_2 following a spin single-qubit rotation $|D\rangle \to \cos(\varphi)|0\rangle + \sin(\varphi)|D\rangle$[40–42] with φ a rotation angle, and hold for another τ_0 for a Hadamard operation. Therefore, this Hadamard gate is in a quantum superposition of being both present and absent. The three steps correspond, respectively, to the input beam-splitter, the phase shifter and the quantum output beam-splitter acting in sequence on a single photon in the Mach–Zehnder interferometer, as shown in Fig. 1a. The final state of the system therefore becomes

$$|\Psi\rangle_f = \cos(\varphi)|\mathrm{particle}\rangle|0\rangle + \sin(\varphi)|\mathrm{wave}\rangle|D\rangle, \tag{16}$$

where

$$|\mathrm{particle}\rangle = \frac{1}{\sqrt{2}}\left[\exp(i\phi)b_1^\dagger + ib_2^\dagger\right]|\mathrm{vac}\rangle, \tag{17}$$

$$|\mathrm{wave}\rangle = \frac{1}{2}\left\{[\exp(i\phi) - 1]b_1^\dagger + i[\exp(i\phi) + 1]b_2^\dagger\right\}|\mathrm{vac}\rangle, \tag{18}$$

describe the particle and wave behaviors, respectively. The coherent evolution of the system is given in more detail in Supplementary Section 2. We find from Eq. (16) that the mechanical phonon is in a quantum superposition of both a wave and a particle, and thus can exhibit both characteristics simultaneously. By applying microwave pulse sequences to tune the rotation angle φ, an arbitrary wave-particle superposition state can be prepared on demand. In the case of $\varphi = 0$, the single phonon behaves completely as a particle, but as a wave for $\varphi = \pi/2$. The morphing between them can also be observed by tuning the rotation angle φ. The probability, P_k, of finding a phonon in the kth CNT is given by

$$P_k = \frac{1}{2} + (-1)^k\frac{1}{2}\sin^2(\varphi)\cos(\phi), \tag{19}$$

which includes two physical contributions, one from the particle nature and the other from the wave nature. Note that the spin in a mixed state $\cos^2(\varphi)|0\rangle\langle 0| + \sin^2(\varphi)|D\rangle\langle D|$ is capable of reproducing the same measured statistics as in Eq. (19).[11] Thus, in order to exclude the classical interpretation and prove the existence of the coherent wave-particle superposition, the quantum coherence between the states $|0\rangle$ and $|D\rangle$ should be verified.[19,20,24,25] Experimentally, such a verification can be implemented by performing quantum state tomography to show all elements of the density matrix of the spin.[42]

Next, we consider how to initialize and measure the mechanical system. Initially, the NV spin needs to be in the state $|D\rangle$ (i.e., the ground state of the spin qubit), one CNT, e.g., the first CNT, needs to be in its single-phonon state, and the other CNT, e.g., the second CNT, needs to be in its vacuum state. To prepare such an initial state, we can begin with an arbitrary state $\rho_{\mathrm{ini}} = \rho_1 \otimes \rho_2 \otimes \rho_{\mathrm{spin}}$, where ρ_k ($k = 1, 2$) and ρ_{spin} are the density matrices of the kth CNT resonator and the spin, respectively. One can apply a 532 nm laser pulse to initialize the spin qubit in the state $|0\rangle$, and then apply a microwave $\pi/2$-pulse to it, to obtain the superposition state $\frac{1}{\sqrt{2}}(|0\rangle + |-1\rangle)$, which is followed by a microwave π-pulse to obtain the spin-qubit excited state $|B\rangle$. By using the sideband-cooling technique,[43–47] the CNT resonators can be cooled down to their quantum ground state, i.e., the acoustic vacuum $|\mathrm{vac}\rangle$. For example, one can couple an auxiliary qubit with a large spontaneous-emission rate to the CNT resonators.[48] Once the mechanical ground state is achieved, one can tune the spin-qubit transition frequency ω_q to be close to the CNT resonance frequency ω_m, such that the spin-CNT coupling is then approximately given by a Jaynes–Cummings-type Hamiltonian

$$H_{\mathrm{int}} \simeq \hbar g\left(\sigma_+ b_1 + \sigma_- b_1^\dagger\right). \tag{20}$$

When acting for a time equal to $\pi/(2g)$, such a Hamiltonian can, with the spin qubit in the excited state $|B\rangle$, transfer a mechanical excitation to the left CNT.[49] Meanwhile, the spin qubit goes to its ground state $|D\rangle$. The desired initial state $|\Psi\rangle_i = \left(b_1^\dagger \otimes \mathcal{I}_2|\mathrm{vac}\rangle\right) \otimes |D\rangle$ is then obtained. For the phonon number measurement, we still need $\omega_q \simeq \omega_m$ as in the initialization, but the spin qubit is required to be in the ground state $|D\rangle$. In this situation, the Rabi frequency between the spin and the mechanical resonator depends on the number of phonons in the resonator.[49–53] Thus by directly measuring the occupation probability of $|B\rangle$, the phonon number in each CNT can be obtained. The measurement of the spin state is enabled by the different fluorescence of the states $|0\rangle$ and $|\pm 1\rangle$.[54] To measure the state of the spin qubit, one can first apply a microwave π pulse to map $|D\rangle \to \frac{1}{\sqrt{2}}(|0\rangle - |-1\rangle)$ and $|B\rangle \to \frac{1}{\sqrt{2}}(|0\rangle + |-1\rangle)$, and then apply a microwave $\pi/2$ pulse to map $\frac{1}{\sqrt{2}}(|0\rangle - |-1\rangle) \to |0\rangle$ and $\frac{1}{\sqrt{2}}(|0\rangle + |-1\rangle) \to |-1\rangle$. By measuring the Rabi oscillations between the states $|0\rangle$ and $|-1\rangle$ according to spin-state-dependent fluorescence,[55] one can read-out the spin-qubit state. If one employs the repetitive-readout technique with auxiliary nuclear spins, the readout fidelity can be further improved.[56]

Mechanical noise

Before discussing the mechanical noise, we need to analyze the total operation time, $\tau_T = 2\tau_0 + \tau_1$, required for our quantum delayed-choice experiment. Note that during τ_T, we have neglected the spin single-qubit operation time due to the driving pulse length ~ns.[57,58] Since $0 \le \tau_1 \le 2\pi/J$, we focus on the maximum τ_T: $\tau_T^{\max} = 5\pi/(2J)$. A modest spin-CNT coupling $g/2\pi = 100$ kHz, which can be obtained by tuning the current I and the distance d (see Supplementary Section 1), is able to mediate an effective CNT–CNT coupling $J/2\pi \simeq 12$ kHz, thus giving $\tau_T^{\max} \simeq 0.1$ ms. The relaxation time T_1 of a single NV spin at low temperatures can reach up to a few minutes. Moreover, with spin echo techniques, a single spin in an ultra-pure diamond example typically has a dephasing time $T_2 \simeq 2$ ms even at room temperature,[59] corresponding to a dephasing rate $\gamma_s/2\pi \simeq 80$ Hz. When dynamical decoupling pulse sequences are employed, the dephasing time can be made even close to one second at low temperatures.[60] These justify neglecting the spin decoherence. In this case, the mechanical noise dominates the dissipative processes. The dynamics of the system is therefore governed by

the following master equation,

$$\dot{\rho}(t) = \frac{i}{\hbar}[\rho(t), H(t)] - \frac{\gamma_m}{2} n_{\rm th} \sum_{k=1,2} \mathcal{L}\left(b_k^\dagger\right)\rho(t) - \frac{\gamma_m}{2}(n_{\rm th}+1) \sum_{k=1,2} \mathcal{L}(b_k)\rho(t), \tag{21}$$

where $\rho(t)$ is the density operator of the system, γ_m is the mechanical decay rate, $n_{\rm th} = [\exp(\hbar\omega_m/k_B T) - 1]^{-1}$ is the equilibrium phonon occupation at temperature T, and $\mathcal{L}(o)\rho(t) = o^\dagger o\rho(t) - 2o\rho(t)o^\dagger + \rho(t)o^\dagger o$ is the Lindblad superoperator. Here, $H(t)$ is a binary Hamiltonian of the form,

$$H(t) = \begin{cases} H_0, & 0 < t \le \tau_0, \text{ and } \tau_0 + \tau_1 < t \le \tau_T \\ H_1, & \tau_0 < t \le \tau_0 + \tau_1, \end{cases} \tag{22}$$

with

$$H_0 = J\left(\sum_{k=1,2} b_k^\dagger b_k + b_1 b_2^\dagger + b_2 b_1^\dagger\right)\sigma_z \tag{23}$$

and $H_1 = Jb_1^\dagger b_1 \sigma_z$. In Eq. (22), we did not include the spin single-qubit operation before the third time interval because the length of the driving pulse is very short, as mentioned above. The master equation in Eq. (21) drives the phonon occupation of the kth CNT to be

$$n_k = \langle b_k^\dagger b_k\rangle(\tau_T) = P_k \exp(-\gamma_m\tau_T) + n_{\rm th}[1 - \exp(-\gamma_m\tau_T)], \tag{24}$$

at time $t = \tau_T$. For a realistic CNT, we can set the mechanical linewidth to be $\gamma_m/2\pi = 0.4$ Hz,[61] leading to a single-phonon lifetime of $\tau_m = 1/\gamma_m \simeq 400$ ms. In this situation, τ_m is much longer than the total operation time τ_T, $\gamma_m\tau_T \ll 1$, and, thus, we obtain

$$n_k = P_k + n_{\rm th}\gamma_m\tau_T. \tag{25}$$

This shows that, in addition to the coherent signal P_k, the final occupation has a thermal contribution $n_{\rm th}\gamma_m\tau_T$. In Fig. 2, we demonstrate the morphing behavior between particle and wave at $T \simeq 10$ mK, according to Eq. (25). To confirm this, we also plot numerical simulations, which are in exact agreement with our analytical expression. The thermal occupation, $n_{\rm th}\gamma_m\tau_T$, increases as the phase ϕ, because such a phase arises from the dynamical accumulation as discussed above. However, an extremely long phonon lifetime causes it to become negligible even at finite temperatures, as shown in Fig. 2.

We now consider the fluctuation noise. In the limit $\gamma_m\tau_T \ll 1$, the fluctuation noise $\delta n_k^{\rm noise}$ in the phonon occupation n_k is expressed, according to the analysis in the Supplementary Section 4, as

$$\left(\delta n_k^{\rm noise}\right)^2 = P_k(2P_k - 1)\gamma_m\tau_m + (2P_k + 1)n_{\rm th}\gamma_m\tau_T, \tag{26}$$

where the first term is the vacuum fluctuation, which can be neglected, and the second term is the thermal fluctuation, which increases with temperature. To quantitatively describe the ability to resolve the coherent signal from the fluctuation noise, we typically employ the signal-to-noise ratio defined as

$$\mathcal{R}_k = \frac{P_k}{\delta n_k^{\rm noise}}. \tag{27}$$

The signal-resolved regime often requires $\mathcal{R}_k > 1$ for any P_k. However, the probability P_k in the range zero to unity indicates that there always exist some P_k such that $\mathcal{R}_k < 1$, in particular, at finite temperatures. Nevertheless, we find that the total fluctuation noise

$$\mathcal{S}^2 = \left(\delta n_1^{\rm noise}\right)^2 + \left(\delta n_2^{\rm noise}\right)^2 \tag{28}$$

is kept below an upper bound

$$\mathcal{B}^2 = \gamma_m\tau_T^{\rm max} + 4n_{\rm th}\gamma_m\tau_T^{\rm max}, \tag{29}$$

and further that assuming $\mathcal{B}^2 < 1/2$ can make either or both of $\mathcal{R}_1$ and $\mathcal{R}_2$ greater than 1. In this case, at least one CNT signal is resolved for each measurement. The conservation of the coherent phonon number equal to 1 ensures that the unresolved signal can be inferred from the resolved one, which allows the morphing between wave and particle to be effectively observed from the fluctuation noise. To quantify this, we define a signal visibility as,

$$\mathcal{R} = \frac{\sqrt{2}}{2\mathcal{B}}, \tag{30}$$

in analogy to the signal-to-noise ratio $\mathcal{R}_k$. The ratio $\mathcal{R}$ describes the visibility of the total signal rather than the single CNT signals. At zero temperature ($n_{\rm th} = 0$), the noise originates only from the vacuum fluctuation, and this yields $\mathcal{R} \gg 1$. However, at finite temperatures, $n_{\rm th}$ increases as T, causing a decrease in $\mathcal{R}$, as shown in Fig. 3. Therefore, the requirement of $\mathcal{R} > 1$ sets an upper bound on the temperature, and as a result, leads to a critical

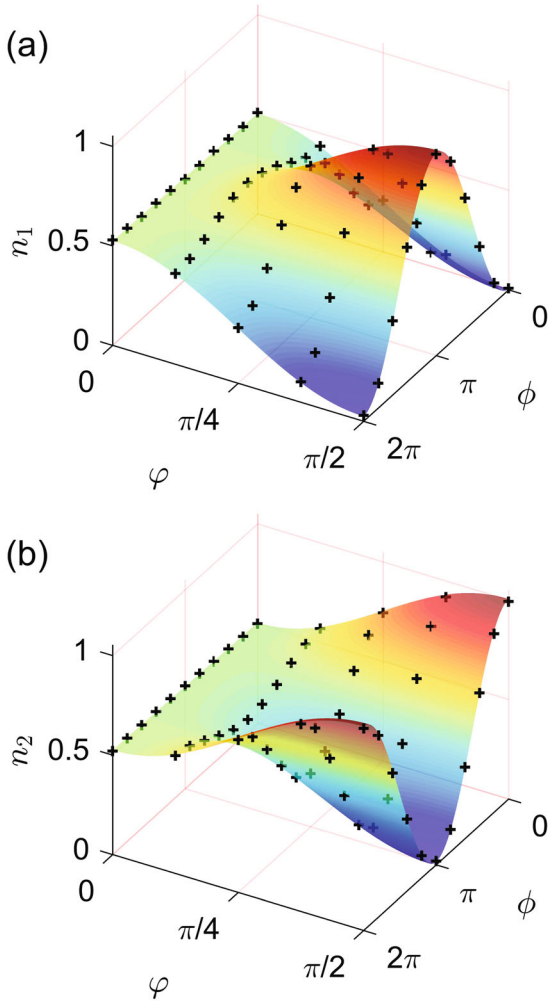

Fig. 2 Morphing between particle and wave characteristics of a CNT mechanical phonon. Phonon occupation **a** n_1 and **b** n_2 as a function of the relative phase ϕ and the rotation angle φ. The analytical results (colored surfaces) are in excellent agreement with the numerical simulations (black symbols). Here, in addition to $\gamma_s/2\pi = 200\gamma_m/2\pi = 80$ Hz, we assume that $g/2\pi = 100$ kHz, $\omega_m/2\pi = 2$ MHz, $\Omega = 10\omega_m$, and $\Delta_- = 142\omega_m$, resulting in $\omega_q \simeq 1.5\omega_m$ and then $J/2\pi \simeq \times 12$ kHz, and that $n_{\rm th} = 100$, corresponding to an environmental temperature of ≃10 mK

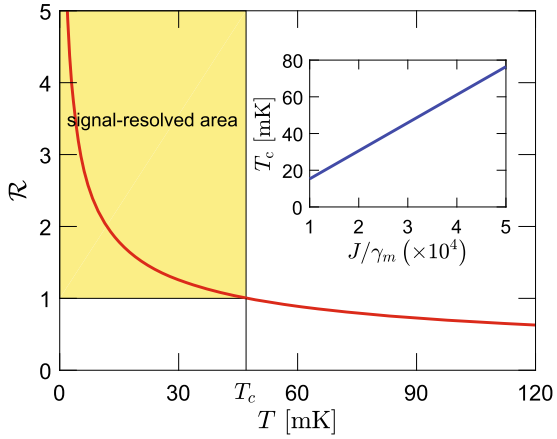

Fig. 3 Signal visibility $\mathcal{R}$ as a function of the temperature T. The yellow shaded area represents the signal-resolved regime, where the morphing between wave and particle can be effectively observed in the fluctuation noise. The vertical line corresponds to the critical temperature T_c. The inset shows a linear increase in T_c with increasing the ratio of the spin-mediated CNT–CNT coupling strength J to the mechanical-mode decay rate γ_m. Here, all parameters are set to be the same as in Fig. 2

temperature,

$$T_c = \frac{\hbar\omega_m}{k_B \ln[(1+15\pi\gamma_m/J)/(1-5\pi\gamma_m/J)]}. \tag{31}$$

The critical temperature linearly increases with J/γ_m, as plotted in the inset of Fig. 3. To increase J, we can increase the current I through the CNTs, decrease the distance d between the CNTs, or decrease the spin-qubit transition frequency ω_q. Furthermore, the increase in the CNT resonance frequency ω_m or the decrease in the CNT loss rate γ_m can also lead to an increase in the critical temperature. For modest parameters of $J/2\pi = 12$ kHz and $\gamma_m/2\pi = 0.4$ Hz, a critical temperature T_c of $\simeq$47 mK, which is routinely accessible in current experiments, can be achieved.

Test of macroscopicity

We have described the implementation of a quantum paradox with massive mechanical objects with experimentally distinguishable single-phonon excitations. The question arises whether this proposal can be considered as a test of macroscopicity.[62,63] Typical proposals of such tests (as cited below) have been based on implementing superpositions of macroscopically distinguishable states of classical-like systems, which are often referred to as Schrödinger's cat states (see, e.g., ref. [64]). Sometimes, the meaning of Schrödinger's cat states is limited to "superposition states of macroscopic systems, where the amplitude of their excitations is large".[65] Note, however, that the term "large amplitude" can be understood in various ways. These include the cases (criteria) when (i) the amplitudes of the constituent states of a given superposition are large as in classical systems, or (ii) when these amplitudes are large enough concerning their experimental distinguishability (i.e., compared to the resolution of detectors). Strictly speaking, a state satisfying one of these conditions, does not necessarily satisfy the other. For example, a superposition of coherent states, $|\psi\rangle = \mathcal{N}(|\alpha\rangle + |\beta\rangle)$ with $\mathcal{N}$ being a normalization constant, is a cat state according to criterion (i) if $|\alpha|, |\beta| \gg 1$, but cannot be considered as a cat state according to criterion, (ii) if $\epsilon \equiv |\alpha - \beta| \ll 1$ is beyond the resolution of detectors. Conversely, $|\psi\rangle$ is a cat state according to criterion (ii) if ϵ can be resolved experimentally even if $|\alpha|, |\beta| \approx 1$, i.e., when criterion (i) is not satisfied. In the latter case, when the amplitude of such excitations is not large in classical terms, but still macroscopically distinguishable, the states are sometimes referred to as Schrödinger's kitten states, as, e.g., those generated and measured in ref. [66]. In this sense, the single-phonon wave-particle superposition, given in Eq. (16), can be referred to as a Schrödinger kitten state, since the excitations of the macroscopic mechanical systems are small, i.e., at the single-phonon level. Indeed, the amplitudes of single-phonon excitations are not large enough to satisfy criterion (i). However, such superpositions of single phonons are large enough that the constituent states of the superposition, given in Eqs. (17) and (18), are experimentally distinguishable, thus satisfying criterion (ii). Therefore, such a test of a quantum principle at the low-excitation level of massive mechanical objects can also be viewed as a test at the macroscopic scale, as claimed, e.g., in refs. [67–69] and references therein.

We note that a collective degree of freedom of many atoms does not necessarily imply that the system is in a macroscopic quantum state. However, we showed that the studied system of macroscopic resonators can be in a maximally entangled two-mode state. This state is described by a non-positive Glauber–Sudarshan P function. This implies that the system itself is quantum. Below we describe the method to amplify the small-excitation kitten states, given in Eqs. (17) and (18), to a cat state with large excitation.

Amplification of the Schrödinger kitten states

Here we apply the idea and method of ref. [70] to show how to amplify the phonon numbers of the single-phonon superposition states $|\text{particle}\rangle$ and $|\text{wave}\rangle$, given in Eqs. (17) and (18), by squeezing the mechanical modes b_1 and b_2. Thus, these states can become Schrödinger's cat-like states. For simplicity, but without loss of generality, here we consider a squeezing operator

$$U_k = \exp\left[\frac{r}{2}\left(b_k^{\dagger 2} - b_k^2\right)\right], \tag{32}$$

acting on the mode b_k ($k = 1, 2$), with r being a squeezing parameter. This squeezing leads to

$$|S_{10}\rangle = \left(U_1 b_1^\dagger \otimes U_2\right)|\text{vac}\rangle = |S_1\rangle_1 |S_0\rangle_2, \tag{33}$$

$$|S_{01}\rangle = \left(U_1 \otimes U_2 b_2^\dagger\right)|\text{vac}\rangle = |S_0\rangle_1 |S_1\rangle_2, \tag{34}$$

where we have defined the phonon squeezed Fock states $|S_0\rangle_k = U_k|0\rangle_k$ and $|S_1\rangle_k = U_k b_k^\dagger |0\rangle_k$, with $|0\rangle_k$ being the vacuum state of the mechanical-mode b_k. As a result, the states $|\text{particle}\rangle$ and $|\text{wave}\rangle$ become

$$|\mathcal{P}_r\rangle = \frac{1}{\sqrt{2}}[\exp(i\phi)|S_{10}\rangle + i|S_{01}\rangle], \tag{35}$$

$$|\mathcal{W}_r\rangle = \frac{1}{2}\{[\exp(i\phi) - 1]|S_{10}\rangle + i[\exp(i\phi) + 1]|S_{01}\rangle\}, \tag{36}$$

respectively. The final state $|\Psi\rangle_f$ becomes

$$|\Psi\rangle_f = \cos(\varphi)|\mathcal{P}_r\rangle|0\rangle + \sin(\varphi)|\mathcal{W}_r\rangle|D\rangle. \tag{37}$$

The modes b_k for $k = 1, 2$ are transformed, via squeezing, to the Bogoliubov modes described by

$$U_k^\dagger b_k U_k = \cosh(r) b_k + \sinh(r) b_k^\dagger. \tag{38}$$

By using this unitary transformation, one obtains the average phonon numbers of $|S_0\rangle_k$ and $|S_1\rangle_k$ equal to

$${}_k\langle S_0|b_k^\dagger b_k|S_0\rangle_k = \sinh^2(r), \tag{39}$$

$${}_k\langle S_1|b_k^\dagger b_k|S_1\rangle_k = 3\sinh^2(r) + 1. \tag{40}$$

We note that by applying this unconditional amplification method, one can exponentially increase the distinguishability of the states $|S_{10}\rangle$ and $|S_{01}\rangle$. Although, a single-shot distinguishability of the mechanical-mode states $|\mathcal{P}_r\rangle$ and $|\mathcal{W}_r\rangle$ is *not* increased, a tomographic distinguishability of these states in the phase space

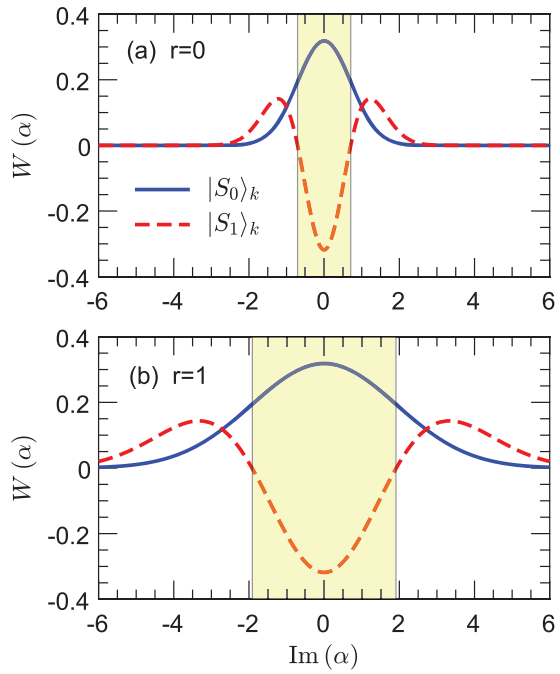

Fig. 4 Wigner function for the states $|S_0\rangle_k = U_k|0\rangle_k$ (solid curves) and $|S_1\rangle_k = U_k|1\rangle_k$ (dashed curves) for $r = 0$ in **a** and 1 in **b**. Here, $k = 1, 2$. The Wigner function is defined as $W(\alpha) = \pi^{-2}\int d^2\beta \exp(-i\beta\alpha^* - i\beta^*\alpha)\mathrm{Tr}\left[\exp(i\beta^* a)\exp\left(i\beta a^\dagger\right)\varrho\right]$. For both plots, we have assumed $\mathrm{Re}(\alpha) = 0$. It is seen that the region marked in yellow, corresponding to the negative Wigner function for $|S_1\rangle_k$, increases with increasing squeezing parameter r

is increased with the amplified amplitudes of the mechanical-mode excitations. Indeed, the distinguishability of $|\mathcal{P}\rangle_r$ and $|\mathcal{W}_r\rangle$, as measured by the infidelity, $\mathrm{IF} = 1 - |\langle\mathcal{W}_r|\mathcal{P}_r\rangle|^2 = 1 - |\langle\mathrm{wave}|\mathrm{particle}\rangle|^2$, is independent of the squeezing parameter r for a given ϕ. For any $\phi \neq \pm\pi/2$, the states are distinguishable, and the highest distinguishability is for $\phi = 0,\pi$, for which the infidelity is $\mathrm{IF} = 1/2$. Thus, even for such optimal values of ϕ, it is impossible to deterministically distinguish the states $|\mathcal{P}_r\rangle$ and $|\mathcal{W}_r\rangle$ from each other in a single-shot experiment. We refer to this property as a single-shot distinguishability. Anyway, these mechanical states can be macroscopically distinguished by performing, e.g., Wigner-function tomography on a number of their copies. Such tomographic distinguishability in phase space indeed increases with the squeezing parameter r, as shown in Fig. 4.

Finally, we note that the famous optical prototypes of the Schrödinger's cat states, which are given by the odd and even coherent states, $|\psi_\pm\rangle = \mathcal{N}(|\alpha\rangle \pm |-\alpha\rangle)$, cannot be distinguished deterministically in a single-shot experiment either. This is because the coherent states $|\alpha\rangle$ and $|-\alpha\rangle$ are not orthogonal for finite values of α. Their overlap decreases exponentially with increasing α, so $|\alpha\rangle$ and $|-\alpha\rangle$ become orthogonal in the limit of large $|\alpha|$. However, this amplification of α cannot be done deterministically, because this process is prohibited by the no-cloning and no-signalling theorems. Indeed, non-orthogonal states cannot be deterministically transformed to orthogonal (thus, completely distinguishable) states. Note that popular methods of amplifying small-amplitude states are based on either (i) probabilistic but accurate amplification or (ii) deterministic but inaccurate cloning. For example, the method described, e.g., in refs. [66,71] is probabilistic, because it is based on conditional measurements performed on two copies of $|\psi_\pm\rangle$. In contrast to this, the amplification method in ref. [70], as applied here, corresponds to approximate quantum cloning, i.e., phase-covariant cloning by stimulated emission.

DISCUSSION

We have presented a proposal for a quantum delayed-choice experiment with nanomechanical resonators, which enables a macroscopic test of an arbitrary quantum wave-particle superposition. The ability to tolerate the mechanical noise has also been given here, demonstrating that our proposal can be implemented with current experimental techniques. While we have chosen to focus on a spin-nanomechanical setup, the present method could be directly extended to other hybrid systems, for example, mechanical devices coupled to a superconducting atom.[32,49,72] Recently, an experimental work reported that photons can be entangled in their wave-particle degree of freedom.[22] This indicates that the wave-particle nature of photons may be used to encode flying qubits for long-distance quantum communication. Photons are ideal quantum information carriers, but they are difficult to store. In contrast to photons, long-lived phonons could be used for optical information storage.[73] Our study shows that phonons can also be prepared in a wave-particle superposition state, and that the wave-particle nature of phonons is not more special than their other degrees of freedom. Thus, the wave-particle degree of freedom of phonons may be exploited for storing quantum information encoded in the wave-particle degree of freedom of photons. In addition, optomechanical interactions can couple a mechanical mode to optical modes at different frequencies.[74] Thus, the mechanical wave-particle degree of freedom may be employed to map quantum information encoded in the wave-particle degree of freedom from photons at a given frequency to photons at any desired frequency. The mechanical wave-particle nature, as a new degree of freedom, may find various applications in quantum information.

We believe that the macroscopicity of our single-phonon wave-particle superposition is highly counter-intuitive, as based on a refined version of the quantum paradox, even if the mechanical resonators are in the single-phonon-excitation regime. Indeed, we analyzed a "nested" kitten state, as given in Eq. (16), where the particle and wave states, given in Eqs. (17) and (18), are purely mechanical kitten states for $\phi \neq \pm\pi/2$. Moreover, we have described a method, based on mechanical-mode squeezing, which enables the amplification of small-excitation Schrödinger kitten states, given in Eqs. (17) and (18), to large-excitation Schrödinger cat states of the massive mechanical resonators. For these reasons, an experimental realization of our proposal can be a fundamental test of a coherent wave-particle superposition of massive objects with phonon excitations, which can be increased exponentially by squeezing. Hence, this proposed quantum delayed-choice experiment of massive mechanical resonators not only leads to a better understanding of quantum theory at the macroscopic scale, but also indicates that, like the vertical and horizontal polarizations of photons, the mechanical wave-particle nature, as an additional degree of freedom of phonons, may be widely exploited for quantum information applications.

DATA AVAILABILITY

The data that supports the findings of this study are available in the Supplementary Information file. Additional data are also available from the corresponding authors upon reasonable request.

ACKNOWLEDGEMENTS

W.Q. thanks Peng-Bo Li for valuable discussions. W.Q. and J.Q.Y. were supported in part by the National Key Research and Development Program of China (Grant No. 2016YFA0301200), the China Postdoctoral Science Foundation (Grant No. 2017M610752), and the NSFC (Grant No. 11774022). G.L.L. is supported in part by

National Key Research and Development Program of China (2017YFA0303700); Beijing Advanced Innovation Center for Future Chip (ICFC). A.M. and F.N. acknowledge the support of a grant from the John Templeton Foundation. F.N. is supported in part by the: MURI Center for Dynamic Magneto-Optics via the Air Force Office of Scientific Research (AFOSR) (FA9550-14-1-0040), Army Research Office (ARO) (Grant No. Grant No. W911NF-18-1-0358), Asian Office of Aerospace Research and Development (AOARD) (Grant No. FA2386-18-1-4045), Japan Science and Technology Agency (JST) (Q-LEAP program, ImPACT program, and CREST Grant No. JPMJCR1676), Japan Society for the Promotion of Science (JSPS) (JSPS-RFBR Grant No. 17-52-50023, and JSPS-FWO Grant No. VS.059.18N), and RIKEN-AIST Challenge Research Fund.

AUTHOR CONTRIBUTIONS

W.Q. and A.M. developed the theory and performed the calculations. G.L.L., J.Q.Y., and F. N. supervised the project. All authors researched, collated, and wrote this paper.

ADDITIONAL INFORMATION

Supplementary information accompanies the paper on the *npj Quantum Information* website (https://doi.org/10.1038/s41534-019-0172-9).

Competing interests: The authors declare no competing interests.

Publisher's note: Springer Nature remains neutral with regard to jurisdictional claims in published maps and institutional affiliations.

REFERENCES

1. Bohr, N. in *Quantum Theory and Measurement*, (eds Wheeler, J. A. & Zurek, W. H.) 9–49 (Princeton University Press, Princeton, 1984).
2. Wheeler, J. A. in *Mathematical Foundations of Quantum Theory*, (eds Marlow, A. R.) 9–48 (Academic Press, Cambridge, 1978).
3. Ma, X.-s, Kofler, J. & Zeilinger, A. Delayed-choice gedanken experiments and their realizations. *Rev. Mod. Phys.* **88**, 015005 (2016).
4. Hellmuth, T., Walther, H., Zajonc, A. & Schleich, W. Delayed-choice experiments in quantum interference. *Phys. Rev. A* **35**, 2532 (1987).
5. Kim, Y.-H., Yu, R., Kulik, S. P., Shih, Y. & Scully, M. O. Delayed "Choice" Quantum Eraser. *Phys. Rev. Lett.* **84**, 1 (2000).
6. Jacques, V. et al. Experimental realization of Wheeler's delayed-choice gedanken experiment. *Science* **315**, 966–968 (2007).
7. Jacques, V. et al. Delayed-choice test of quantum complementarity with interfering single photons. *Phys. Rev. Lett.* **100**, 220402 (2008).
8. Manning, A. G., Khakimov, R. I., Dall, R. G. & Truscott, A. G. Wheeler's delayed-choice gedanken experiment with a single atom. *Nat. Phys.* **11**, 539 (2015).
9. Liu, Y., Lu, J. & Zhou, L. Information gain versus interference in Bohr's principle of complementarity. *Opt. Express* **25**, 202–211 (2017).
10. Vedovato, F. et al. Extending Wheeler's delayed-choice experiment to space. *Sci. Adv.* **3**, e1701180 (2017).
11. Chaves, R., Lemos, G. B. & Pienaar, J. Causal modeling the delayed-choice experiment. *Phys. Rev. Lett.* **120**, 190401 (2018).
12. Ionicioiu, R. & Terno, D. R. Proposal for a quantum delayed-choice experiment. *Phys. Rev. Lett.* **107**, 230406 (2011).
13. Adesso, G. & Girolami, D. Quantum optics: wave-particle superposition. *Nat. Photon.* **6**, 579 (2012).
14. Shadbolt, P., Mathews, J. C. F., Laing, A. & O'Brien, J. L. Testing foundations of quantum mechanics with photons. *Nat. Phys.* **10**, 278 (2014).
15. Roy, S. S., Shukla, A. & Mahesh, T. S. NMR implementation of a quantum delayed-choice experiment. *Phys. Rev. A* **85**, 022109 (2012).
16. Auccaise, R. et al. Experimental analysis of the quantum complementarity principle. *Phys. Rev. A* **85**, 032121 (2012).
17. Xin, T., Li, H., Wang, B.-X. & Long, G.-L. Realization of an entanglement-assisted quantum delayed-choice experiment. *Phys. Rev. A* **92**, 022126 (2015).
18. Tang, J.-S. et al. Realization of quantum Wheeler's delayed-choice experiment. *Nat. Photon.* **6**, 600–604 (2012).
19. Peruzzo, A., Shadbolt, P., Brunner, N., Popescu, S. & O'Brien, J. L. A quantum delayed-choice experiment. *Science* **338**, 634–637 (2012).
20. Kaiser, F., Coudreau, T., Milman, P., Ostrowsky, D. B. & Tanzilli, S. Entanglement-enabled delayed-choice experiment. *Science* **338**, 637–640 (2012).
21. Yan, H. et al. Experimental observation of simultaneous wave and particle behavior in a narrowband single-photon wave packet. *Phys. Rev. A* **91**, 042132 (2015).
22. Rab, A. S. et al. Entanglement of photons in their dual wave-particle nature. *Nat. Commun.* **8**, 915 (2017).
23. Long, G.-L., Qin, W., Yang, Z. & Li, J.-L. Realistic interpretation of quantum mechanics and encounter-delayed-choice experiment. *Sci. China Phys. Mech. Astron.* **61**, 030311 (2018).
24. Zheng, S.-B. et al. Quantum delayed-choice experiment with a beam splitter in a quantum superposition. *Phys. Rev. Lett.* **115**, 260403 (2015).
25. Liu, K. et al. A twofold quantum delayed-choice experiment in a superconducting circuit. *Sci. Adv.* **3**, e1603159 (2017).
26. Blencowe, M. Quantum electromechanical systems. *Phys. Rep.* **395**, 159–222 (2004).
27. Aspelmeyer, M., Kippenberg, T. J. & Marquardt, F. Cavity optomechanics. *Rev. Mod. Phys.* **86**, 1391 (2014).
28. Poot, M. & van der Zant, H. S. J. Mechanical systems in the quantum regime. *Phys. Rep.* **511**, 273–335 (2012).
29. Iijima, S. Helical microtubules of graphitic carbon. *Nature* **354**, 56 (1991).
30. Liu, D. E. Sensing Kondo correlations in a suspended carbon nanotube mechanical resonator with spin-orbit coupling. *Quantum Eng.* **1**, e10 (2019).
31. Buluta, I., Ashhab, S. & Nori, F. Natural and artificial atoms for quantum computation. *Rep. Prog. Phys.* **74**, 104401 (2011).
32. Xiang, Z. L., Ashhab, S., You, J. Q. & Nori, F. Hybrid quantum circuits: superconducting circuits interacting with other quantum systems. *Rev. Mod. Phys.* **85**, 623 (2013).
33. Rabl, P. et al. Strong magnetic coupling between an electronic spin qubit and a mechanical resonator. *Phys. Rev. B* **79**, 041302 (2009).
34. Rabl, P. et al. A quantum spin transducer based on nanoelectromechanical resonator arrays. *Nat. Phys.* **6**, 602 (2010).
35. Kolkowitz, S. et al. Coherent sensing of a mechanical resonator with a single-spin qubit. *Science* **335**, 1603–1606 (2012).
36. Li, P.-B., Xiang, Z.-L., Rabl, P. & Nori, F. Hybrid quantum device with nitrogen-vacancy centers in diamond coupled to carbon nanotubes. *Phys. Rev. Lett.* **117**, 015502 (2016).
37. Cao, P., Betzholz, R., Zhang, S. & Cai, J. Entangling distant solid-state spins via thermal phonons. *Phys. Rev. B* **96**, 245418 (2017).
38. Gamel, O. & James, D. F. V. Time-averaged quantum dynamics and the validity of the effective Hamiltonian model. *Phys. Rev. A* **82**, 052106 (2010).
39. Qin, W. et al. Exponentially enhanced light-matter interaction, cooperativities, and steady-state entanglement using parametric amplification. *Phys. Rev. Lett.* **120**, 093601 (2018).
40. Huang, P. et al. Observation of an anomalous decoherence effect in a quantum bath at room temperature. *Nat. Commun.* **2**, 570 (2011).
41. Lillie, S. E. et al. Environmentally mediated coherent control of a spin qubit in diamond. *Phys. Rev. Lett.* **118**, 167204 (2017).
42. Xing, J. et al. Experimental investigation of quantum entropic uncertainty relations for multiple measurements in pure diamond. *Sci. Rep.* **7**, 2563 (2017).
43. Xue, F., Wang, Y. D., Liu, Y.-x & Nori, F. Cooling a micromechanical beam by coupling it to a transmission line. *Phys. Rev. B* **76**, 205302 (2007).
44. You, J. Q., Liu, Y.-x & Nori, F. Simultaneous cooling of an artificial atom and its neighboring quantum system. *Phys. Rev. Lett.* **100**, 047001 (2008).
45. Grajcar, M., Ashhab, S., Johansson, J. R. & Nori, F. Lower limit on the achievable temperature in resonator-based sideband cooling. *Phys. Rev. B* **78**, 035406 (2008).
46. Ma, Y., Yin, Z.-q, Huang, P., Yang, W. L. & Du, J. F. Cooling a mechanical resonator to the quantum regime by heating it. *Phys. Rev. A* **94**, 053836 (2016).
47. Clark, J. B., Lecocq, F., Simmonds, R. W., Aumentado, J. & Teufel, J. D. Sideband cooling beyond the quantum backaction limit with squeezed light. *Nature* **541**, 191–195 (2017).
48. Wang, X., Miranowicz, A., Li, H.-R. & Nori, F. Hybrid quantum device with a carbon nanotube and a flux qubit for dissipative quantum engineering. *Phys. Rev. B* **95**, 205415 (2017).
49. O'Connell, A. D. et al. Quantum ground state and single-phonon control of a mechanical resonator. *Nature* **464**, 697 (2010).
50. Scully, M. O. & Zubairy, M. S. *Quantum Optics*. (Cambridge University Press, Cambridge, 1997).
51. Liu, Y.-x, Wei, L. F. & Nori, F. Generation of nonclassical photon states using a superconducting qubit in a microcavity. *Europhys. Lett.* **67**, 941 (2004).
52. Hofheinz, M. et al. Generation of Fock states in a superconducting quantum circuit. *Nature* **454**, 310 (2008).
53. Hofheinz, M. et al. Synthesizing arbitrary quantum states in a superconducting resonator. *Nature* **459**, 546 (2009).
54. Doherty, M. W. et al. The nitrogen-vacancy colour centre in diamond. *Phys. Rep.* **528**, 1–45 (2013).
55. Jelezko, F., Gaebel, T., Popa, I., Gruber, A. & Wrachtrup, J. Observation of coherent oscillations in a single electron spin. *Phys. Rev. Lett.* **92**, 076401 (2004).
56. Jiang, L. et al. Repetitive readout of a single electronic spin via quantum logic with nuclear spin ancillae. *Science* **326**, 267–272 (2009).
57. Liu, G.-Q. et al. Demonstration of entanglement-enhanced phase estimation in solid. *Nat. Commun.* **6**, 6726 (2015).

58. Liu, G.-Q. et al. Single-shot readout of a nuclear spin weakly coupled to a nitrogen-vacancy center at room temperature. *Phys. Rev. Lett.* **118**, 150504 (2017).
59. Balasubramanian, G. et al. Ultralong spin coherence time in isotopically engineered diamond. *Nat. Mater.* **8**, 383–387 (2009).
60. Bar-Gill, N., Pham, L. M., Jarmola, A., Budker, D. & Walsworth, R. L. Solid-state electronic spin coherence time approaching one second. *Nat. Commun.* **4**, 1743 (2013).
61. Moser, J., Eichler, A., Güttinger, J., Dykman, M. I. & Bachtold, A. Nanotube mechanical resonators with quality factors of up to 5 million. *Nat. Nanotechnol.* **9**, 1007–1011 (2014).
62. Leggett, A. J. Testing the limits of quantum mechanics: motivation, state of play, prospects. *J. Phys.* **14**, R415 (2002).
63. Korsbakken, J. I., Whaley, K. B., Dubois, J. & Cirac, J. I. Measurement-based measure of the size of macroscopic quantum superpositions. *Physi. Rev. A* **75**, 042106 (2007).
64. Gerry, C. & Knight, P. *Introductory Quantum Optics*. (Cambridge University Press, Cambridge, 2005).
65. Agarwal, G. S. *Quantum Optics*. (Cambridge University Press, Cambridge, 2013).
66. Ourjoumtsev, A., Tualle-Brouri, R., Laurat, J. & Grangier, P. Generating optical Schrödinger kittens for quantum information processing. *Science* **312**, 83–86 (2006).
67. Hofer, S. G., Lehnert, K. W. & Hammerer, K. Proposal to Test Bell's Inequality in Electromechanics. *Phys. Rev. Lett.* **116**, 070406 (2016).
68. Marinković, I. et al. Optomechanical bell test. *Phys. Rev. Lett.* **121**, 220404 (2018).
69. Ockeloen-Korppi, C. F. et al. Stabilized entanglement of massive mechanical oscillators. *Nature* **556**, 478 (2018).
70. Sekatski, P., Brunner, N., Branciard, C., Gisin, N. & Simon, C. Towards quantum experiments with human eyes as detectors based on cloning via stimulated emission. *Phys. Rev. Lett.* **103**, 113601 (2009).
71. Lund, A. P., Jeong, H., Ralph, T. C. & Kim, M. S. Conditional production of superpositions of coherent states with inefficient photon detection. *Phys. Rev. A* **70**, 020101(R) (2004).
72. Gu, X., Kockum, A. F., Miranowicz, A., Liu, Y.-x & Nori, F. Microwave photonics with superconducting quantum circuits. *Phys. Rep.* **718–719**, 1–102 (2017).
73. Fiore, V. et al. Storing optical information as a mechanical excitation in a silica optomechanical resonator. *Phys. Rev. Lett.* **107**, 133601 (2011).
74. Dong, C., Fiore, V., Kuzyk, M. C. & Wang, H. Optomechanical dark mode. *Science* **338**, 1609–1613 (2012).

Supplementary information for: Proposal to Test Quantum Wave-Particle Superposition on Massive Mechanical Resonators

Wei Qin,[1,2] Adam Miranowicz,[1,3] Guilu Long,[4] J. Q. You,[5,2] and Franco Nori[1,6]

[1] *Theoretical Quantum Physics Laboratory, RIKEN Cluster for Pioneering Research, Wako-shi, Saitama 351-0198, Japan*
[2] *Quantum Physics and Quantum Information Division, Beijing Computational Science Research Center, Beijing 100193, China*
[3] *Faculty of Physics, Adam Mickiewicz University, 61-614 Poznań, Poland*
[4] *State Key Laboratory of Low-Dimensional Quantum Physics and Department of Physics, Tsinghua University, Beijing 100084, China*
[5] *Department of Physics and State Key Laboratory of Modern Optical Instrumentation, Zhejiang University, Hangzhou 310027, China*
[6] *Department of Physics, The University of Michigan, Ann Arbor, Michigan 48109-1040, USA*

Here, we, first, in Sec. I present more details of how to obtain the spin-controlled coherent coupling between separated mechanical resonators. Second, in Sec. II, we show the detailed implementation of the controlled Hadamard gate, the phase gate, and the mechanical quantum delayed-choice experiment. Next, in Sec. III, we derive in detail the phonon occupation of each CNT at finite temperatures. Then, Sec. IV describes the detailed derivation of the fluctuation noise and the detailed analysis of the requirement of resolving the coherent signal from the environment-induced fluctuation. Finally, in Sec. V we show the method of the numerical simulation used in this work.

I. Spin-controlled coherent coupling between separated mechanical resonators

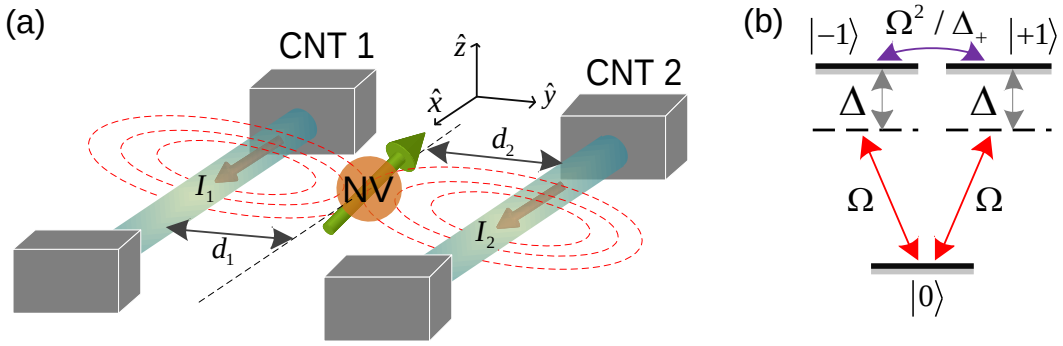

FIG. 1. (Color online) (a) Schematic representation of a mechanical quantum delayed-choice experiment with an NV electronic spin and two carbon nanotubes (CNTs). The mechanical vibrations of the CNTs, labelled by $k = 1, 2$, are completely decoupled or coherently coupled, depending, respectively, on whether or not the intermediate spin is in the spin state $|0\rangle$, with the dc current I_k through the kth CNT, and the distance d_k between the spin and the kth CNT. (b) Level structure of the driven NV spin in the electronic ground state. Here we have assumed that the Zeeman splitting between the spin states $|\pm 1\rangle$ is eliminated by applying an external field.

The effective Hamiltonian $H_{\rm eff}$ in the article describes a spin-mediated CNT-CNT coupling conditioned on the NV spin state. This is the basic element underlying our proposal. To understand more explicitly the spin-controlled coupling between the CNTs, in this section we derive in detail the effective Hamiltonian. We consider a hybrid quantum system consisting of two parallel CNTs and an NV electronic spin (a qutrit), as depicted in Fig. 1(a). Here, for convenience, illustrations in Figs. 1(b) and 1(c) in the article are reproduced in Figs. 1(b) and 1(a), respectively. The CNTs, respectively, carry dc currents I_1 and I_2, both along the $+\hat{x}$–direction. A spin is placed between them, at a distance d_1 (d_2) from the first (second) CNT. According to the Biot-Savart law, the CNTs can, at the position of the spin, generate a magnetic field $\vec{B}^{(0)}_{\rm cnt} = B^{(0)}_{\rm cnt}\hat{z}$, where

$$B^{(0)}_{\rm cnt} = \sum_{k=1,2} (-1)^{k-1} \frac{\mu_0 I_k}{2\pi d_k}, \tag{1}$$

$\hat{\epsilon}$ ($\epsilon = x, y, z$) is a unit vector in the $\hat{\epsilon}$–direction, μ_0 is the vacuum permeability, and the subscript "cnt" refers to the CNTs. When the CNTs vibrate along the $\hat{y}$-direction, the magnetic field is parametrically modulated by their mechanical displacements y_1 and y_2, and then is reexpressed, up to first order, as $\vec{B}_{\rm cnt} = \vec{B}^{(0)}_{\rm cnt} + \vec{B}^{(1)}_{\rm cnt}$, where $\vec{B}^{(1)}_{\rm cnt} = B^{(1)}_{\rm cnt}\hat{z}$ is a first-order modification, and where $B^{(1)}_{\rm cnt} = \sum_{k=1,2} G_k y_k$, with a magnetic-field gradient,

$$G_k = \frac{\mu_0 I_k}{2\pi d_k^2}. \tag{2}$$

Note that, here, $y_1 > 0$ ($y_2 < 0$) indicates a decrease in d_1 (d_2). Therefore, the sign, $(-1)^{k-1}$, in Eq. (1) does not appear in Eq. (2). Furthermore, an external magnetic field, $\vec{B}_{\rm ext} = B_x(t)\,\hat{x} + B_z\hat{z}$, is applied to the NV spin. We have assumed, as required below, that $B_x(t)$ is a time-dependent component but B_z is a dc component. The Hamiltonian governing the NV spin is therefore given by

$$H_{\rm NV} = \hbar D S_z^2 + \mu_B g_s \left[B^{(0)}_{\rm cnt} + B_z\right] S_z + \mu_B g_s B_x(t)\, S_x + \mu_B g_s B^{(1)}_{\rm cnt} S_z, \tag{3}$$

where $g_s \simeq 2$ is the Landé factor, μ_B the Bohr magneton, $D \simeq 2\pi \times 2.87$ GHz the zero-field splitting, and S_ϵ the ϵ–component of the spin operator $\vec{S}$ ($\epsilon = x, y, z$). In terms of the eigenstates, $\{|m_s\rangle, m_s = 0, \pm 1\}$, of S_z, the operator S_ϵ is expanded as

$$S_x = \frac{1}{2}\begin{pmatrix} 0 & \sqrt{2} & 0 \\ \sqrt{2} & 0 & \sqrt{2} \\ 0 & \sqrt{2} & 0 \end{pmatrix},\ S_y = \frac{1}{2i}\begin{pmatrix} 0 & \sqrt{2} & 0 \\ -\sqrt{2} & 0 & \sqrt{2} \\ 0 & -\sqrt{2} & 0 \end{pmatrix},\ \text{and}\ \ S_z = \frac{1}{2}\begin{pmatrix} +1 & 0 & 0 \\ 0 & 0 & 0 \\ 0 & 0 & -1 \end{pmatrix}, \tag{4}$$

and accordingly, the Hamiltonian $H_{\rm NV}$ is transformed to

$$\begin{aligned} H_{\rm NV} = &\left\{\hbar D + \mu_B g_s \left[B^{(0)}_{\rm cnt} + B_z\right]\right\} |+1\rangle\langle +1| + \left\{\hbar D - \mu_B g_s \left[B^{(0)}_{\rm cnt} + B_z\right]\right\} |-1\rangle\langle -1| \\ &+ \frac{1}{\sqrt{2}}\mu_B g_s B_x(t)\left(|-1\rangle\langle 0| + |+1\rangle\langle 0| + \text{H.c.}\right) \\ &+ \mu_B g_s B^{(1)}_{\rm cnt}\left(|+1\rangle\langle +1| - |-1\rangle\langle -1|\right). \end{aligned} \tag{5}$$

We find that the magnetic field along the $\hat{z}$–direction causes different Zeeman shifts to be imposed, respectively, on the spin states $|\pm 1\rangle$, and also that the magnetic field along the $\hat{x}$–direction drives the transition between the spin states $|0\rangle$ and$|\pm 1\rangle$.

The quantum treatment of the mechanical motion demonstrates that the mechanical vibrations of the CNTs can be modelled by two single-mode harmonic oscillators with a Hamiltonian

$$H_{\rm mv} = \sum_{k=1,2} \hbar\omega_k b_k^\dagger b_k, \tag{6}$$

where ω_k is the phonon frequency and b_k ($b_k^\dagger$) is the phonon annihilation (creation) operator. Here, we have subtracted the constant zero-point energy $\hbar\omega_k/2$. The mechanical displacement y_k is accordingly expressed as

$$y_k = y^{(k)}_{\rm zp}\left(b_k + b_k^\dagger\right) \equiv y^{(k)}_{\rm zp} q_k, \tag{7}$$

where q_k is the canonical phonon position operator, and $y^{(k)}_{\rm zp} = \left[\hbar/\left(2m_k\omega_k\right)\right]^{1/2}$, with m_k being the effective mass, describes the zero-point (zp) motion. Combining Eqs. (5), (6), and (7) gives the full Hamiltonian of the hybrid system,

$$\begin{aligned} H_F = &\sum_{k=1,2} \hbar\omega_k b_k^\dagger b_k + \left\{\hbar D + \mu_B g_s \left[B^{(0)}_{\rm cnt} + B_z\right]\right\} |+1\rangle\langle +1| \\ &+ \left\{\hbar D - \mu_B g_s \left[B^{(0)}_{\rm cnt} + B_z\right]\right\} |-1\rangle\langle -1| \\ &+ \frac{1}{\sqrt{2}}\mu_B g_s B_x(t)\left(|-1\rangle\langle 0| + |+1\rangle\langle 0| + \text{H.c.}\right) \\ &+ \sum_{k=1,2} \mu_B g_s G_k y^{(k)}_{\rm zp}\left(|+1\rangle\langle +1| - |-1\rangle\langle -1|\right) q_k. \end{aligned} \tag{8}$$

The last line in Eq. (8) describes a magnetic coupling between the spin and the mechanical modes. In order to realize a tunable detuning between them, $B_x(t)$ is chosen to be $B_x(t) = B_0\cos(\omega_0 t)$ with amplitude B_0 and frequency ω_0. In a frame rotating at $H_{\rm rot} = \hbar\omega_0(|-1\rangle\langle -1| + |+1\rangle\langle +1|)$, the full Hamiltonian can be divided into two parts, $H_F = H_{\rm low} + H_{\rm high}$, where

$$\begin{aligned} H_{\rm low} =& \sum_{k=1,2}\hbar\omega_k b_k^\dagger b_k + \hbar\delta_+|+1\rangle\langle +1| + \hbar\delta_-|-1\rangle\langle -1| \\ &+ \hbar\Omega\left(|-1\rangle\langle 0| + |+1\rangle\langle 0| + \text{H.c.}\right) \\ &+ \sum_{k=1,2}\hbar g_k\left(|+1\rangle\langle +1| - |-1\rangle\langle -1|\right)q_k, \end{aligned} \tag{9}$$

$$H_{\rm high} = \hbar\Omega\left[\exp(i2\omega_0 t)\,|-1\rangle\langle 0| + \exp(i2\omega_0 t)\,|+1\rangle\langle 0| + \text{H.c.}\right], \tag{10}$$

account for the low- and high-frequency components, respectively. Here, we have defined

$$\begin{aligned} \hbar\delta_\pm &= \hbar D \pm \mu_B g_s\left[B_{\rm nt}^{(0)} + B_z\right] - \hbar\omega_0, \\ \hbar\Omega &= \frac{1}{2\sqrt{2}}\mu_B g_s B_0, \\ \hbar g_k &= \mu_B g_s G_k y_{\rm zp}^{(k)}. \end{aligned} \tag{11}$$

Roughly, having $\delta'_\pm = \delta_\pm + 2\omega_0 \gg \Omega$ allows one to make the rotating-wave approximation (RWA), and to straightforwardly remove $H_{\rm high}$. However, as demonstrated in Sec. V, the accumulated error increases during the evolution, causing the dynamics driven by $H_{\rm low}$ to deviate largely from that driven by H_F. Thus, we are *not* using the RWA here. In order to suppress the error accumulation, we need to analyze the effects of $H_{\rm high}$ in the limit $\delta'_\pm \gg \Omega$. In such a limit, we can employ a time-averaging treatment for the high-frequency component $H_{\rm high}$ [1, 2], and as a result, its effective behavior is described by the following time-averaged Hamiltonian,

$$\begin{aligned} \overline{H}_{\rm high} =& \hbar\left(\frac{2\Omega^2}{\delta'_-} + \frac{\Omega^2}{\delta'_+}\right)|-1\rangle\langle -1| + \hbar\left(\frac{\Omega^2}{\delta'_-} + \frac{2\Omega^2}{\delta'_+}\right)|+1\rangle\langle +1| \\ &+ \hbar\frac{\Omega^2}{2}\left(\frac{1}{\delta'_-} + \frac{1}{\delta'_+}\right)\left\{\exp\left[i\left(\delta_- + \delta'_- - \delta_+ - \delta'_+\right)t\right]|-1\rangle\langle +1| + \text{H.c.}\right\}, \end{aligned} \tag{12}$$

where the first line corresponds to the energy shifts of the spin states $|\pm 1\rangle$, and the second line describes a coherent coupling between these. Accordingly, the full Hamiltonian H_F is approximated to be a time-independent form,

$$H_F \simeq H_{\rm low} + \overline{H}_{\rm high}. \tag{13}$$

As seen in Sec. V, the error accumulation is strongly suppressed when $\overline{H}_{\rm high}$ is included.

Tuning $B_{\rm cnt}^{(0)} + B_z = 0$ yields $\delta_+ = \delta_- = \Delta_-$ and $\delta'_+ = \delta'_- = \Delta_+$, implying that the spin states $|\pm 1\rangle$ have the same Zeeman shift of $\Delta = \Delta_- + 3\Omega^2/\Delta_+$, as shown in Fig. 1(b). Therefore, we can define a bright state, $|B\rangle = (|+1\rangle + |-1\rangle)/\sqrt{2}$, which is dressed by the spin state $|0\rangle$, and a dark state, $|D\rangle = (|+1\rangle - |-1\rangle)\sqrt{2}$, which decouples from the spin state $|0\rangle$. In terms of the states $|B\rangle$ and $|D\rangle$, the full Hamiltonian becomes

$$\begin{aligned} H_F \simeq& \sum_{k=1,2}\hbar\omega_k b_k^\dagger b_k + \hbar\Delta\left(|B\rangle\langle B| + |D\rangle\langle D|\right) + \hbar\sqrt{2}\Omega\left(|0\rangle\langle B| + |B\rangle\langle 0|\right) \\ &+ \sum_{k=1,2}\hbar g_k\left(|B\rangle\langle D| + |D\rangle\langle B|\right)q_k + \hbar\frac{\Omega^2}{\Delta_+}\left(|B\rangle\langle B| - |D\rangle\langle D|\right). \end{aligned} \tag{14}$$

The dressing mechanism allows us to introduce two dressed states,

$$|\Phi_-\rangle = \cos(\theta)\,|0\rangle - \sin(\theta)\,|B\rangle, \tag{15}$$

$$|\Phi_+\rangle = \sin(\theta)\,|0\rangle + \cos(\theta)\,|B\rangle, \tag{16}$$

where $\tan(2\theta) = 2\sqrt{2}\Omega/\Delta$. Upon substituting them back into the full Hamiltonian in Eq. (14) and then using the

identity operator $\mathcal{I} = |D\rangle\langle D| + |\Phi_-\rangle\langle\Phi_-| + |\Phi_+\rangle\langle\Phi_+|$, we can straightforwardly obtain

$$\begin{aligned} H_F \simeq & \sum_{k=1,2} \hbar\omega_k b_k^\dagger b_k + \hbar\omega_+ |\Phi_+\rangle\langle\Phi_+| + \hbar\omega_D |D\rangle\langle D| \\ & + \sum_{k=1,2} \hbar \left[g_k^{(-)} |\Phi_-\rangle\langle D| + g_k^{(+)} |D\rangle\langle\Phi_+| + \text{H.c.} \right] q_k \\ & + \hbar \frac{\Omega^2}{\Delta_+} \left[\cos(2\theta) |\Phi_+\rangle\langle\Phi_+| - \frac{1}{2}\sin(2\theta) \left(|\Phi_+\rangle\langle\Phi_-| + \text{H.c.} \right) - \cos^2(\theta) |D\rangle\langle D| \right]. \end{aligned} \tag{17}$$

Here,

$$\omega_+ = \sqrt{\Delta^2 + 8\Omega^2}, \tag{18}$$

$$\omega_D = \frac{1}{2}\left(\Delta + \sqrt{\Delta^2 + 8\Omega^2} \right), \tag{19}$$

$$g_k^{(-)} = -g_k \sin(\theta), \tag{20}$$

$$g_k^{(+)} = g_k \cos(\theta). \tag{21}$$

Under the assumption of $\Delta \gg \Omega$, we have $\theta \simeq 0$, such that $\sin(\theta) \simeq \sin(2\theta) \simeq 0$, $\cos(\theta) \simeq \cos^2(\theta) \simeq \cos(2\theta) \simeq 1$, $\omega_+ \simeq \Delta + 4\Omega^2/\Delta$, $\omega_D \simeq \Delta + 2\Omega^2/\Delta$, and $|\Phi_+\rangle \simeq |B\rangle$. In this limit, the coupling between $|0\rangle$ and $|B\rangle$ only causes an energy splitting, of $\simeq 2\Omega^2/\Delta$, between the states $|B\rangle$ and $|D\rangle$, so $|B\rangle$ and $|D\rangle$ can be used to define a spin qubit. Correspondingly, the full Hamiltonian is approximated as

$$H_F' = \sum_{k=1,2} \hbar\omega_k b_k^\dagger b_k + \frac{1}{2}\hbar\omega_q \sigma_z + \sum_{k=1,2} \hbar g_k \sigma_x q_k, \tag{22}$$

where $\omega_q = 2\Omega^2/\Delta + 2\Omega^2/\Delta_+$, $\sigma_z = |B\rangle\langle B| - |D\rangle\langle D|$, and $\sigma_x = \sigma_+ + \sigma_-$ with $\sigma_- = |D\rangle\langle B|$ and $\sigma_+ = \sigma_-^\dagger$. Modest parameters [3–9], $m_k = 1.0 \times 10^{-22}$ kg, $\omega_k/2\pi = 2$ MHz, $d_k \simeq 2$ nm, and $I_k \simeq 380$ nA, could result in a spin-CNT coupling of up to $g_k/2\pi \simeq 100$ kHz.

Furthermore, from Eq. (22) it is found that the sequential actions of the terms $\sigma_+ b_1$ and $\sigma_- b_2^\dagger$, as well as of the counter-rotating terms $\sigma_- b_1$ and $\sigma_+ b_2^\dagger$, can transfer a mechanical phonon from the left to the right CNT, and the reverse process is caused by their Hermitian conjugates. When restricting our discussion to a dispersive regime,

$$\omega_q \pm \omega_k \gg |g_k|, \tag{23}$$

this phonon transfer becomes dominant. Hence, in the dispersive regime the dynamics described by H_F' in Eq. (22) enables a spin quantum bus for the mechanical phonons and can be used to realize a coherent CNT-CNT coupling. In order to show more explicitly, we rewrite H_F' in the interaction picture as

$$H_F' = \sum_{k=1,2} \hbar g_k \left\{ \sigma_+ b_k \exp\left[i(\omega_q - \omega_k) \right] + \sigma_+ b_k^\dagger \exp\left[i(\omega_q + \omega_k) \right] + \text{H.c.} \right\}. \tag{24}$$

The condition in Eq. (23) justifies to use a time-averaging treatment of the Hamiltonian H_F' [1, 2]. In the time-averaging treatment, all terms in Eq. (24) are considered as high-frequency components and exhibit time-averaged behaviors. Based on this, the dynamics of the system can be determined by an effective Hamiltonian

$$H_{\text{eff}} = \frac{2\hbar\omega_q}{\omega_q^2 - \omega_m^2} \left[\sum_{k=1,2} g_k^2 b_k^\dagger b_k + g_1 g_2 \left(b_1 b_2^\dagger + b_2 b_1^\dagger \right) \right] \otimes \sigma_z. \tag{25}$$

Here, we have assumed that $\omega_k = \omega_m$. As expected, Eq. (25) shows a coherent spin-mediated CNT-CNT coupling, corresponding to the standard linear coupler transformation, which can give rise to a direct phonon exchange. Thus in this case, the spin qubit works as a quantum bus. At the same time, it also shows that the CNT-CNT coupling can be turned off if the intermediate spin is in the state $|0\rangle$. This is because the NV spin in the state $|0\rangle$ is decoupled from the CNTs, and the mechanical phonons can no longer be transferred from one CNT to another. Specifically, if the spin is in the state $|D\rangle$ or $|B\rangle$, the CNTs are coupled; however, if the spin is instead in the state $|0\rangle$, they are decoupled. Note that in Eq. (25) ac Stark shifts caused to be imposed on the qubit have been excluded because we focus only on the quantum states of the CNTs.

In the last part of this section, we evaluate the direct coupling between the CNTs. For simplicity, we assume that $I_k = I$, $d_k = d$, and that the CNTs have the same length L. The attractive force acting on the kth CNT is

$$\vec{F}_k = (-1)^{k-1} F \hat{y}, \tag{26}$$

where

$$F = \frac{\mu_0 L I^2}{2\pi (d - y_1 + y_2)} \tag{27}$$

is the force size. The work done by the force is given straightforwardly by

$$W = \frac{\mu_0 L I^2 (y_1 - y_2)}{2\pi (d - y_1 - y_2)}. \tag{28}$$

After applying a perturbation expansion and then a quantization, this direct CNT-CNT coupling is found to be

$$\begin{aligned} W =& \hbar W^{(1)} (b_1 - b_2 + \text{H.c.}) \\ &+ \hbar W^{(2)} \left[\left(b_1 + b_1^\dagger \right)^2 + \left(b_2 + b_2^\dagger \right)^2 - 2 \left(b_1 + b_1^\dagger \right) \left(b_2 + b_2^\dagger \right) \right], \end{aligned} \tag{29}$$

where

$$W^{(1)} = \frac{\mu_0 L I^2 y_{\text{zp}}}{2\pi d \hbar}, \tag{30}$$

$$W^{(2)} = \frac{\mu_0 L I^2 y_{\text{zp}}^2}{2\pi d^2 \hbar}. \tag{31}$$

For a modest setup [3–9], $m = 1.0 \times 10^{-22}$ kg, $\omega_m = 2\pi \times 2$ MHz, $L = 10$ nm, $d = 2$ nm, and $I = 380$ nA, we have

$$W^{(1)} \simeq 2\pi \times 20 \text{ kHz}, \tag{32}$$

which is much smaller than the mechanical resonance frequency ω_m, and also have

$$W^{(2)} \simeq 2\pi \times 1 \text{ kHz}, \tag{33}$$

which is much smaller than the spin-mediated CNT-CNT coupling, for example, $\simeq 2\pi \times 12$ kHz, as shown in the section below. Therefore, the direct CNT-CNT coupling can be neglected in our setup.

II. Controlled Hadamard gate, phase gate, and mechanical quantum delayed-choice experiment

In order to implement a quantum delayed-choice experiment with macroscopic CNT mechanical resonators, we need a controlled Hadamard gate and a phase gate to act on the CNT mechanical modes. Below, we demonstrate how the effective Hamiltonian in Eq. (25) can be used to make all required gates. Let us first consider the controlled Hadamard gate. Tuning the currents to be $I_k = I$ and, at the same time, the distances to be $d_k = d$ results in a symmetric coupling $g_k = g$. The effective Hamiltonian H_{eff} is accordingly reduced to $H_{\text{eff}} = H_{\text{cnt}} \otimes \sigma_z$, where

$$H_{\text{cnt}} = \hbar J \left(\sum_{k=1,2} b_k^\dagger b_k + b_1 b_2^\dagger + b_2 b_1^\dagger \right) \tag{34}$$

is a beam-splitter-type interaction, and where

$$J = \frac{2 g^2 \omega_q}{\omega_q^2 - \omega_m^2} \tag{35}$$

is an effective CNT-CNT coupling strength. In our discussion, the NV spin is restricted to a subspace spanned by $\{|0\rangle, |D\rangle\}$, where the spin is a control qubit of a Hadamard gate. The spin in the state $|D\rangle$ mediates the coherent coupling between the separated CNTs, and causes them to evolve under the Hamiltonian H_{cnt} in Eq. (34). According

to the Heisenberg equation of motion, $b_k(t) = \exp(iH_{\rm cnt}t/\hbar)\, b_k \exp(-iH_{\rm cnt}t/\hbar)$, the unitary evolution for a time $t = \tau_0 \equiv \pi/(4J)$ corresponds to a Hadamard-like gate,

$$b_1(\tau_0) = \frac{1}{\sqrt{2}}(b_1 - ib_2), \tag{36}$$

$$b_2(\tau_0) = \frac{1}{\sqrt{2}}(b_2 - ib_1). \tag{37}$$

However, when the spin state is $|0\rangle$, the two CNTs decouple from each other. In this case, their quantum states remain unchanged under the unitary evolution, yielding

$$b_1(t) = b_1, \tag{38}$$

$$b_2(t) = b_2. \tag{39}$$

We have therefore achieved a spin-controlled Hadamard gate between the CNTs. That is, if the NV spin is in the state $|D\rangle$, then the Hadamard operation is applied to the CNTs, and if the NV spin is in the state $|0\rangle$, then the states of the CNTs are unchanged.

We next consider the phase gate. For the phase gate, we tune the currents to be $I_1 \neq 0$ and $I_2 = 0$, such that $g_1 = g$ and $g_2 = 0$, causing the effective Hamiltonian in Eq. (25) to become

$$H_{\rm cnt} = \hbar J b_1^\dagger b_1 \sigma_z. \tag{40}$$

We find from Eq. (40) that there exists a spin-induced shift, J, of the mechanical resonance. This dispersive shift can, in turn, introduce a dynamical phase, $\phi(t) = Jt$, onto the first CNT. With the spin being in the state $|D\rangle$, we solve the Heisenberg equations of motion for the CNTs, and then obtain a phase gate,

$$b_1(t) = \exp[i\phi(t)]\, b_1, \tag{41}$$

$$b_2(t) = b_2. \tag{42}$$

In fact, similar to the controlled Hadamard gate discussed above, the phase gate can also be controlled by the spin according to Eq. (40).

Having achieved all required gates, we now turn to the detailed description of the macroscopic quantum delayed-choice experiment with CNT resonators. The hybrid system is initially prepared in the state $|\Psi\rangle_i \equiv |\Psi(0)\rangle = \left(b_1^\dagger \otimes \mathcal{I}_2|{\rm vac}\rangle\right) \otimes |D\rangle$, where $|{\rm vac}\rangle$ refers to the phonon vacuum of the CNTs and $\mathcal{I}_2$ is the identity operator on the second CNT. First, we turn on the currents of the CNTs and ensure $I_k = I$. After a time τ_0, a Hadamard operation is applied to the CNTs and accordingly, $|\Psi\rangle_i$ becomes

$$|\Psi(\tau_0)\rangle = \frac{1}{\sqrt{2}}\left(b_1^\dagger + ib_2^\dagger\right)|{\rm vac}\rangle|D\rangle. \tag{43}$$

Then, we turn off the current of the second CNT for a phase accumulation for a time τ_1. As a consequence, the system further evolves to

$$|\Psi(\tau_0+\tau_1)\rangle = \frac{1}{\sqrt{2}}\left[\exp(i\phi)\, b_1^\dagger + ib_2^\dagger\right]|{\rm vac}\rangle|D\rangle. \tag{44}$$

While achieving the desired phase ϕ, we make a spin single-qubit rotation $|D\rangle \to \cos(\varphi)|0\rangle + \sin(\varphi)|D\rangle$, and have

$$|\Psi(\tau_0+\tau_1)\rangle = \frac{1}{\sqrt{2}}\left[\exp(i\phi)\, b_1^\dagger + ib_2^\dagger\right]|{\rm vac}\rangle\left(\cos\varphi|0\rangle + \sin\varphi|D\rangle\right). \tag{45}$$

Here, note that, we have ignored the length of the driving pulse of the spin rotation as being of the order of ns, and thus assumed that the state of the CNTs remains unchanged. At the end of the driving pulse, we turn on the current of the second CNT again and hold for another τ_0 to perform a Hadamard gate. This gate is in a quantum superposition of being present and absent. The three operations on the mechanical phonon correspond to the actions, on a single photon, of the input beam splitter, the phase shifter, and the output beam splitter, respectively, in quantum delayed-choice experiments with a Mach-Zehnder interferometer. The final state is therefore given by

$$|\Psi\rangle_f \equiv |\Psi(2\tau_0+\tau_1)\rangle = \cos(\varphi)\,|{\rm particle}\rangle|0\rangle + \sin(\varphi)\,|{\rm wave}\rangle|D\rangle, \tag{46}$$

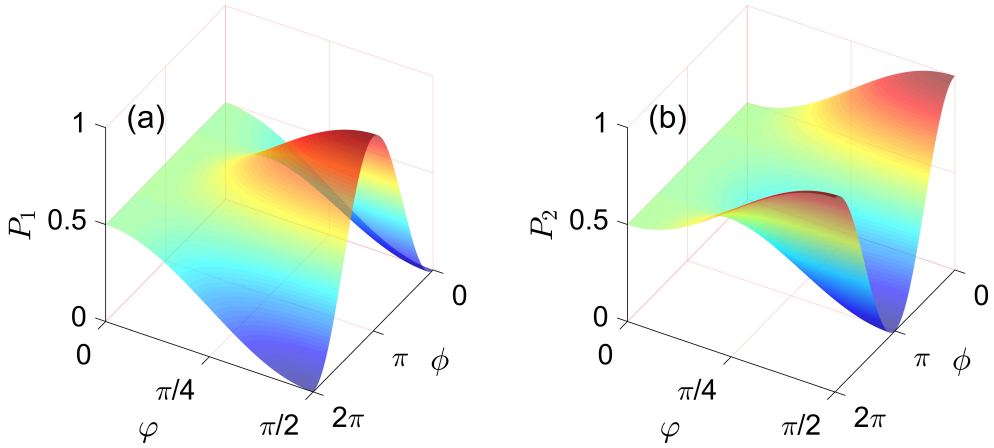

FIG. 2. (Color online) (a) Probability P_1 and (b) P_2 as a function of the rotation angle φ and the relative phase ϕ. This represents a continuous transition between a particle-type behavior ($\varphi = 0$) and a wave-type behavior ($\varphi = \pi/2$).

where

$$|\text{particle}\rangle = \frac{1}{\sqrt{2}}\left[\exp(i\phi)\, b_1^\dagger + i b_2^\dagger\right]|\text{vac}\rangle, \tag{47}$$

$$|\text{wave}\rangle = \frac{1}{2}\left\{\left[\exp(i\phi) - 1\right] b_1^\dagger + i\left[\exp(i\phi) + 1\right] b_2^\dagger\right\}|\text{vac}\rangle, \tag{48}$$

describe particle and wave behaviors, respectively. This reveals that the CNT mechanical phonon is in a quantum superposition of both a particle and a wave. The probability of finding a single phonon in the kth CNT is expressed as

$$P_k = \frac{1}{2} + (-1)^k \frac{1}{2}\sin^2(\varphi)\cos(\phi), \tag{49}$$

according to Eq. (46). In Fig. 2, we have plotted the probabilities P_1 and P_2 versus the rotation angle φ and the relative phase ϕ. In this figure we find that the mechanical phonon shows a morphing behavior between particle ($\varphi = 0$) and wave ($\varphi = \pi/2$).

We now consider the timing errors of the Hadamard and phase gates. We first consider the Hadamard gate. We assume that the error of the time required for performing the Hadamard gate is δ_0, such that the actual evolution time for the gate becomes $\tau_0' = \tau_0 + \delta_0$. In order to estimate the effect of this timing error on the gate performance, we introduce a gate fidelity, defined as

$$\mathcal{F}_0 = \langle \Psi_{\text{target},0}|\rho_{\text{actual},0}(\tau_0')|\Psi_{\text{target},0}\rangle, \tag{50}$$

where $|\Psi_{\text{target},0}\rangle$ is the target state given by the ideal Hadamard gate, and $\rho_{\text{actual},0}(\tau_0')$ is the actual state obtained by integrating the exact master equation, given by Eq. (122). In Fig. 3, we plot the gate fidelity, F_0, versus the timing error δ_0 (red curve). In this figure, the initial state for the Hadamard gate is assumed to be $b_1^\dagger|\text{vac}\rangle|D\rangle$, so that the target state is $|\Psi_{\text{target},0}\rangle = \frac{1}{\sqrt{2}}\left(b_1^\dagger + i b_2^\dagger\right)|\text{vac}\rangle|D\rangle$. Here, $|\text{vac}\rangle$ represents the acoustic vacuum state of the CNT resonators. From this figure, we find that for $-0.32\tau_0 \lesssim \delta_0 \lesssim 0.34\tau_0$, the gate fidelity $\mathcal{F}_0$ can be kept above 0.9.

For the phase gate, we assume, as above, that the timing error is δ_1. Thus, the actual evolution time for the phase gate is $\tau_1' = \tau_1 + \delta_1$. We also introduce a gate fidelity, defined as

$$\mathcal{F}_1 = \langle \Psi_{\text{target},1}|\rho_{\text{actual},1}(\tau_1')|\Psi_{\text{target},1}\rangle, \tag{51}$$

where $|\Psi_{\text{target},1}\rangle$ is the target state given by the ideal phase gate, and $\rho_{\text{actual},1}(\tau_1')$ is the actual state obtained from the exact master equation, given in Eq. (122). The gate fidelity $\mathcal{F}_1$ is plotted as a function of the timing error δ_1 in Fig. (3) (blue curve). There, we assumed that the initial state for the phase gate is $\frac{1}{\sqrt{2}}\left(b_1^\dagger + i b_2^\dagger\right)$, and that the phase accumulated is equal to π. The target state $|\Psi_{\text{target},1}\rangle$ is, therefore, given by $\frac{1}{\sqrt{2}}\left(-b_1^\dagger + i b_2^\dagger\right)$. It is seen from this figure that, as long as $-0.15\tau_1 \lesssim \delta_1 \lesssim 0.12\tau_1$, we can obtain the gate fidelity of $\mathcal{F}_1 > 0.9$.

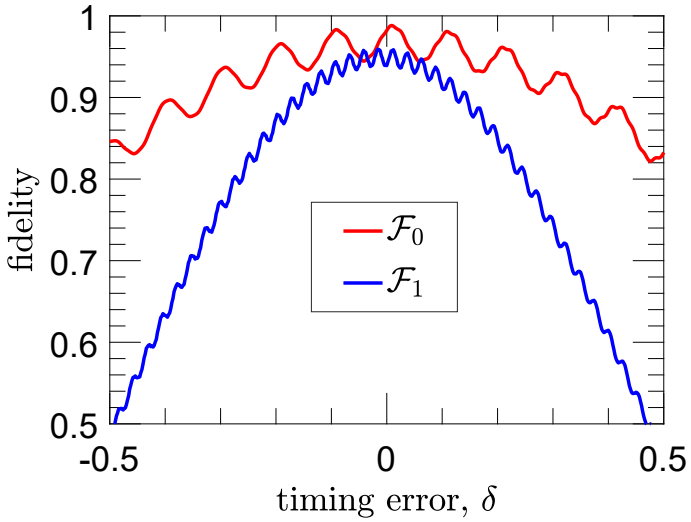

FIG. 3. (Color online) Gate fidelity as a function of the timing error. We have assumed that $\delta_0/\tau_0 = \delta_1/\tau_1 = \delta$, and that the initial state is: (i) $b_1^\dagger|\text{vac}\rangle|D\rangle$ for the Hadamard gate, and (ii) $\frac{1}{\sqrt{2}}\left(b_1^\dagger + ib_2^\dagger\right)|\text{vac}\rangle|D\rangle$ for the phase gate that accumulates a relative phase π. Here, in addition to $\gamma_s/2\pi = 200\gamma_m/2\pi = 80$ Hz, we have assumed that $g/2\pi = 100$ kHz, $\omega_m/2\pi = 2$ MHz, $\Omega = 10\omega_m$, and $\Delta_- = 142\omega_m$, resulting in $\omega_q \simeq 1.5\omega_m$ and then $J/2\pi \simeq 12$ kHz. We have also assumed that $n_{\text{th}} = 100$, which corresponds to the environment temperature of $\simeq 10$ mK.

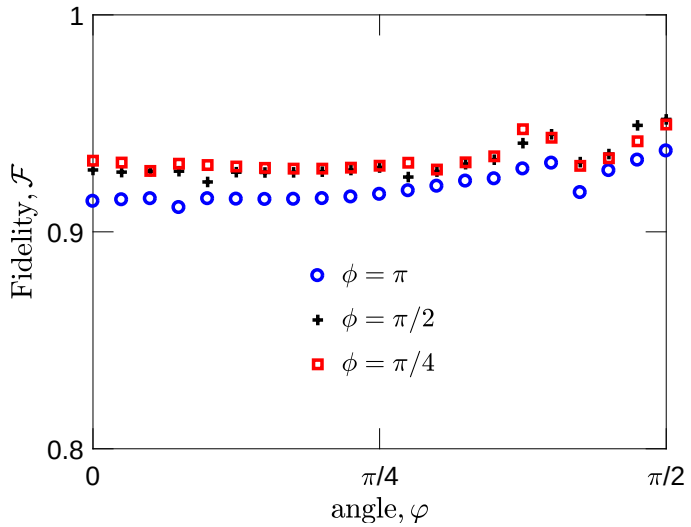

FIG. 4. (Color online) (a) Fidelity $\mathcal{F}$ as a function of the rotation angle φ. All the results are numerically obtained by integrating the exact master equation in Eq. (122). Here, in addition to $\gamma_s/2\pi = 200\gamma_m/2\pi = 80$ Hz, we have assumed that $g/2\pi = 100$ kHz, $\omega_m/2\pi = 2$ MHz, $\Omega = 10\omega_m$, and $\Delta_- = 142\omega_m$, resulting in $\omega_q \simeq 1.5\omega_m$ and then $J/2\pi \simeq 12$ kHz. We have also assumed that $n_{\text{th}} = 100$, which corresponds to an environmental temperature of $\simeq 10$ mK.

Note that the spin, in a classical mixed state of the form $\cos^2(\varphi)\,|0\rangle\langle 0| + \sin^2(\varphi)\,|D\rangle\langle D|$, would lead to the same measured statistics in Eq. (49), that is, a local hidden variable model is capable of reproducing the quantum predictions. This is a loophole [10–13]. However, as discussed in Refs. [14–17], this loophole can be avoided as long as the second Hadamard operation is ensured to be in a truly quantum superposition of being present and absent. In our proposal, the second Hadamard operation is conditioned on the spin state. If the spin is in the $|0\rangle$ state, then the Hadamard operation is absent; if the spin is in the $|D\rangle$ state, then the Hadamard operation is present; if the spin is in a quantum superposition of the $|0\rangle$ and $|D\rangle$ states, then the Hadamard operation is in a quantum superposition of being present and absent. To confirm such a quantum superposition, in Fig. (4) we numerically calculate the fidelity, $\mathcal{F} = {}_f\langle\Psi|\rho_{\text{actual}}(\tau_T)\,|\Psi\rangle_f$, between the desired state $|\Psi\rangle_f$ in Eq. (46) and the actual state $\rho_{\text{actual}}(\tau_T)$ obtained from the exact master equation in Eq. (122). From this figure, we find that the fidelity is very close to unity even for the

finite temperature of $T \simeq 10$ mK. Furthermore, in experiments, in order to exclude the classical interpretation and prove the existence of the coherent wave-particle superposition, the quantum coherence between the states $|0\rangle$ and $|D\rangle$ should be verified. Experimentally, this coherence can be prepared by a spin single-qubit operation [18–20], and can be verified by performing quantum state tomography to show all the elements of the density matrix of the spin [20].

III. Phonon occupation at finite temperatures

We begin by considering the total operation time, which is given by $\tau_T = 2\tau_0 + \tau_1$, as discussed in Sec. II. Here, $\tau_0 = \pi/(4J)$ is the time for the Hadamard gate and $\tau_1 \in [0, 2\pi/J]$ is the time for the phase gate. In a realistic setup, we can assume $\omega_m/2\pi \simeq 2$ MHz, $\omega_q/2\pi \simeq 3$ MHz, and $g/2\pi = 100$ kHz, such that $J/2\pi \simeq 12$ kHz, yielding a maximum total time $\tau_T^{\max} = 2\tau_0 + \tau_1^{\max} \simeq 0.1$ ms, where $\tau_1^{\max} = 2\pi/J$ is the maximum phase gate time. Note that, the operation time τ_T depends inversely on the CNT-CNT coupling strength J, but the enhancement in J is limited by the validity of the effective Hamiltonian H_{eff}.

The total decoherence in our setup can be divided into two parts, one from the spin and the other from the CNTs. The spin decoherence in general includes the relaxation and the dephasing. For an NV electronic spin, the relaxation time T_1 can reach up to several minutes at low temperatures and the dephasing time can be $T_2 \simeq 2$ ms even at room temperature [21, 22]. These justify neglecting the spin decoherence. For the mechanical decoherence, despite a long phonon life, the low mechanical frequency makes the CNT mechanical modes very sensitive to the environmental temperature. In this section and in Sec. IV, we discuss the effects of the mechanical noise on our quantum delayed-choice experiment, and demonstrate that the morphing between wave and particle can still be effectively observed even at finite temperatures.

As a result, the dissipative processes, in the hybrid system considered here, are induced only by the mechanical decoherence, which arises from the vacuum fluctuation and thermal noise. The full dynamics of the system can then be governed by the following master equation

$$\dot{\rho}(t) = \frac{i}{\hbar}[\rho(t), H(t)] - \frac{\gamma_m}{2} n_{\text{th}} \sum_{k=1,2} \mathcal{L}\left(b_k^\dagger\right)\rho(t) - \frac{\gamma_m}{2}(n_{\text{th}}+1)\sum_{k=1,2}\mathcal{L}(b_k)\rho(t), \tag{52}$$

where ρ is the density operator of the system, γ_m is the mechanical decay rate, $n_{\text{th}} = [\exp(\hbar\omega_m/k_B T) - 1]^{-1}$ is the equilibrium phonon occupation at temperature T, and $\mathcal{L}(o)\rho(t) = o^\dagger o\rho(t) - 2o\rho(t)o^\dagger + \rho(t)o^\dagger o$ is the Lindblad superoperator. Here, $H(t)$ is a binary Hamiltonian of the form,

$$H(t) = \begin{cases} H_0, & 0 < t \le \tau_0, \text{ and } \tau_0 + \tau_1 < t \le \tau_T \\ H_1, & \tau_0 < t \le \tau_0 + \tau_1, \end{cases} \tag{53}$$

with

$$H_0 = \hbar J\left(\sum_{k=1,2} b_k^\dagger b_k + b_1 b_2^\dagger + b_2 b_1^\dagger\right)\sigma_z, \tag{54}$$

$$H_1 = \hbar J b_1^\dagger b_1 \sigma_z. \tag{55}$$

The three time intervals in Eq. (53) correspond to the first Hadamard gate, the phase gate and the second Hadamard gate, respectively. Note that in Eq. (53), we did not include the spin single-qubit rotation before the third interval because the length of the driving pulse is of the order of ns. We can derive the system evolution step by step.

Let us now consider the first evolution interval $0 < t \le \tau_0$. During this interval, the coupling of the CNT mechanical modes introduces two delocalized phononic modes,

$$c_\pm = \frac{1}{\sqrt{2}}(b_1 \pm b_2), \tag{56}$$

such that H_0 is diagonalized to be

$$H_0 = 2\hbar J c_+^\dagger c_+ \sigma_z, \tag{57}$$

and the master equation in Eq. (52) is reexpressed, in terms of the modes $c_\pm$, as

$$\dot{\rho} = i\left[\rho, 2Jc_+^\dagger c_+\sigma_z\right] - \frac{\gamma_m}{2} n_{\text{th}} \sum_{\mu=1,2}\mathcal{L}\left(c_\mu^\dagger\right)\rho(t) - \frac{\gamma_m}{2}(n_{\text{th}}+1)\sum_{\mu=1,2} L(c_\mu)\rho(t). \tag{58}$$

In order to calculate the phonon occupations at the end of the first interval, we need to obtain the equations of motion for $\langle c_{\pm}^{\dagger}c_{\pm}\rangle$, $\langle c_{+}^{\dagger}c_{-}\rangle$, $\langle c_{+}^{\dagger}c_{-}\sigma_z\rangle$, and $\langle c_{+}^{\dagger}c_{-}\sigma_z^2\rangle$. Here, $\langle O\rangle$ represents the expectation value of the operator O. Following the master equation in Eq. (58), we have

$$\frac{d}{dt}\langle c_{\pm}^{\dagger}c_{\pm}\rangle = -\gamma_m\langle c_{\pm}^{\dagger}c_{\pm}\rangle + \gamma_m n_{\rm th}, \tag{59}$$

$$\frac{d}{dt}\langle c_{+}^{\dagger}c_{-}\rangle = i2J\langle c_{+}^{\dagger}c_{-}\sigma_z\rangle - \gamma_m\langle c_{+}^{\dagger}c_{-}\rangle, \tag{60}$$

$$\frac{d}{dt}\langle c_{+}^{\dagger}c_{-}\sigma_z\rangle = i2J\langle c_{+}^{\dagger}c_{-}\sigma_z^2\rangle - \gamma_m\langle c_{+}^{\dagger}c_{-}\sigma_z\rangle, \tag{61}$$

$$\frac{d}{dt}\langle c_{+}^{\dagger}c_{-}\sigma_z^2\rangle = i2J\langle c_{+}^{\dagger}c_{-}\sigma_z\rangle - \gamma_m\langle c_{+}^{\dagger}c_{-}\sigma_z^2\rangle, \tag{62}$$

where we have used the relation $\sigma_z^3 = \sigma_z$. We can straightforwardly solve the differential equation (59) to find

$$\langle c_{\pm}^{\dagger}c_{\pm}\rangle(t) = \left(\frac{1}{2} - n_{\rm th}\right)\exp(-\gamma_m t) + n_{\rm th}. \tag{63}$$

Combining Eqs. (61) and (62) gives

$$\langle c_{+}^{\dagger}c_{-}\sigma_z^j\rangle(t) = (-1)^j\,\frac{1}{2}\exp(-i2Jt)\exp(-\gamma_m t), \tag{64}$$

for $j = 1, 2$. Upon substituting Eq. (64) back into Eq. (60), we can then obtain

$$\langle c_{+}^{\dagger}c_{-}\rangle(t) = \frac{1}{2}\exp(-i2Jt)\exp(-\gamma_m t). \tag{65}$$

It is found, according to Eq. (56), that in the localized-mode basis,

$$\langle b_k^{\dagger}b_k\rangle(\tau_0) = \left(\frac{1}{2} - n_{\rm th}\right)\exp(-\gamma_m\tau_0) + n_{\rm th}, \tag{66}$$

$$\langle b_1^{\dagger}b_2\rangle(\tau_0) = \frac{i}{2}\exp(-\gamma_m\tau_0). \tag{67}$$

For the second evolution interval $\tau_0 < t \leq \tau_0 + \tau_1$, we directly use the master equation in Eq. (52) but with $H(t)$ replaced by H_1. When comparing with the master equation in Eq. (58), we see that the equations of motion for $\langle b_k^{\dagger}b_k\rangle$, $\langle b_1^{\dagger}b_2\rangle$, $\langle b_1^{\dagger}b_2\sigma_z\rangle$, and $\langle b_1^{\dagger}b_2\sigma_z^2\rangle$ should have the same forms as in Eqs. (59), (60), (61), and (62), but with the substitutions $c_+ \to b_1$, $c_- \to b_2$ and $2J \to J$. In combination with the initial conditions, given in Eqs. (66) and (67), we follow the same procedure as above to find

$$\langle b_k^{\dagger}b_k\rangle(\tau_0+\tau_1) = \left(\frac{1}{2} - n_{\rm th}\right)\exp[-\gamma_m(\tau_0+\tau_1)] + n_{\rm th}, \tag{68}$$

$$\langle b_1^{\dagger}b_2\rangle(\tau_0+\tau_1) = \frac{i}{2}\exp(-iJ\tau_1)\exp[-\gamma_m(\tau_0+\tau_1)]. \tag{69}$$

We now turn to the third evolution interval $\tau_0 + \tau_1 < t \leq 2\tau_0 + \tau_1$. Before this interval or at the end of the second interval, we apply a single qubit rotation, $|D\rangle \to \cos(\varphi)|0\rangle + \sin(\varphi)|D\rangle$, on the NV spin to engineer the subsequent Hadamard operation to be in a quantum superposition of being absent and present. In this situation, we still use the delocalized-mode basis and the corresponding master equation in Eq. (58). According to Eqs. (68) and (69), the initial conditions of the last evolution can be rewritten, in terms of $c_{\pm}$, as

$$\langle c_{\pm}^{\dagger}c_{\pm}\rangle(\tau_0+\tau_1) = \left[\frac{1}{2} \pm \frac{1}{2}\sin(J\tau_1) - n_{\rm th}\right]\exp[-\gamma(\tau_0+\tau_1)] + n_{\rm th}, \tag{70}$$

$$\langle c_{+}^{\dagger}c_{-}\rangle(\tau_0+\tau_1) = -\frac{i}{2}\cos(J\tau_1)\exp[-\gamma(\tau_0+\tau_1)], \tag{71}$$

$$\langle c_{+}^{\dagger}c_{-}\sigma_z^j\rangle(\tau_0+\tau_1) = (-1)^j\sin^2(\varphi)\langle c_{+}^{\dagger}c_{-}\rangle(\tau_0+\tau_1), \tag{72}$$

for $j = 1, 2$. Then, as before, solving the differential equations in Eqs. (59), (60), (61) and (62) leads to

$$\langle c_{\pm}^{\dagger} c_{\pm} \rangle (t) = \left[\frac{1}{2} \pm \frac{1}{2} \sin (J\tau_1) - n_{\rm th} \right] \exp (-\gamma_m t) + n_{\rm th}, \tag{73}$$

$$\langle c_{+}^{\dagger} c_{-} \rangle (t) = -\frac{i}{2} \cos (J\tau_1) \left\{ \cos^2 (\varphi) + \sin^2 (\varphi) \exp \left[-i2J (t - \tau_0 - \tau_1) \right] \right\} \exp (-\gamma_m t), \tag{74}$$

which, in turn, gives

$$n_k \equiv \langle b_k^{\dagger} b_k \rangle (\tau_T) = (P_k - n_{\rm th}) \exp (-\gamma_m \tau_T) + n_{\rm th}, \tag{75}$$

which is the phonon occupation of the kth at the end of the third interval. For a realistic CNT, the mechanical linewidth can be set to $\gamma_m/2\pi = 0.4$ Hz [23], and then we obtain a phonon lifetime of $\simeq 400$ ms, which is much longer than the maximum total time $\tau_T^{\max} \simeq 0.1$ ms. This ensures $\gamma_m \tau_T \ll 1$, which results in

$$n_k \simeq P_k + n_{\rm th} \gamma_m \tau_T. \tag{76}$$

This shows that the occupation for each CNT has two contributions: one from a coherent phonon signal and one from thermal excitations. Furthermore, we find from Eq. (76) that the thermal excitations have equal contributions to n_1 and n_2. This is because the thermal excitations do not contribute to the interference. For an environmental temperature $T = 10$ mK, the equilibrium phonon occupation is $n_{\rm th} \simeq 100$, yielding $n_{\rm th} \gamma_m \tau_T^{\max} \simeq 0.03$, which can be neglected, as shown in Fig. 2 of the article.

IV. Signal-to-noise ratio at finite temperatures

In addition to the thermal occupation, $n_{\rm th}\gamma_m\tau_T$, in Eq. (76), the desired signal P_k is also always accompanied by fluctuation noise. Such a noise includes vacuum fluctuations and thermal fluctuations. In particular, the latter increases with temperature, so that the signal can be completely drowned in the noise when the temperature is sufficiently high. In this case, it is very difficult to observe the morphing between wave and particle. Thus in this section, we analyze this fluctuation noise in detail, and demonstrate that, in order for the morphing behavior to be observed effectively, the total fluctuation noise of both CNTs should be limited by an upper bound, which leads to a critical temperature T_c.

Specifically, we begin by deriving the fluctuation δn_k in the occupation n_k, for $k = 1, 2$. This is defined by

$$\begin{aligned} (\delta n_k)^2 &= \langle \left(b_k^{\dagger} b_k \right)^2 \rangle (\tau_T) - \langle b_k^{\dagger} b_k \rangle^2 (\tau_T) \\ &= \langle b_k^{\dagger} b_k^{\dagger} b_k b_k \rangle (\tau_T) + n_k - n_k^2. \end{aligned} \tag{77}$$

In order to understand the fluctuation noise better, we need to derive an analytical expression of δn_k. In Sec. III, n_k has been given in Eq. (76). Below, we derive the evolution of $\langle b_k^{\dagger} b_k^{\dagger} b_k b_k \rangle$ in a step-by-step manner as in Sec. III.

We now consider the first evolution interval $0 < t \leq \tau_0$. During this interval, the delocalized modes $c_{\pm}$ in Eq. (56) are employed owing to the coupling of the CNT mechanical modes, and the dynamics is described by the master equation in Eq. (58). To achieve $\langle b_k^{\dagger} b_k^{\dagger} b_k b_k \rangle$ at time τ_T, the dynamical evolutions of $\langle c_{\pm}^{\dagger} c_{\pm}^{\dagger} c_{\pm} c_{\pm} \rangle$, $\langle c_{+}^{\dagger} c_{+} c_{-}^{\dagger} c_{-} \rangle$, $\langle c_{+}^{\dagger} c_{+}^{\dagger} c_{+} c_{-} \rangle$, $\langle c_{+}^{\dagger} c_{-}^{\dagger} c_{-} c_{-} \rangle$, and $\langle c_{+}^{\dagger} c_{+}^{\dagger} c_{-} c_{-} \rangle$ are involved. The equations of motion for $\langle c_{\pm}^{\dagger} c_{\pm}^{\dagger} c_{\pm} c_{\pm} \rangle$ and $\langle c_{+}^{\dagger} c_{+} c_{-}^{\dagger} c_{-} \rangle$ are

$$\frac{d}{dt} \langle c_{\pm}^{\dagger} c_{\pm}^{\dagger} c_{\pm} c_{\pm} \rangle = 4\gamma_m n_{\rm th} \langle c_{\pm}^{\dagger} c_{\pm} \rangle - 2\gamma_m \langle c_{\pm}^{\dagger} c_{\pm}^{\dagger} c_{\pm} c_{\pm} \rangle, \tag{78}$$

$$\frac{d}{dt} \langle c_{+}^{\dagger} c_{+} c_{-}^{\dagger} c_{-} \rangle = \gamma_m n_{\rm th} \left(\langle c_{+}^{\dagger} c_{+} \rangle + \langle c_{-}^{\dagger} c_{-} \rangle \right) - 2\gamma_m \langle c_{+}^{\dagger} c_{+} c_{-}^{\dagger} c_{-} \rangle. \tag{79}$$

Substituting Eq. (63) yields

$$\langle c_{\pm}^{\dagger} c_{\pm}^{\dagger} c_{\pm} c_{\pm} \rangle (\tau_0) = 2X (\tau_0), \tag{80}$$

$$\langle c_{+}^{\dagger} c_{+} c_{-}^{\dagger} c_{-} \rangle (\tau_0) = X (\tau_0), \tag{81}$$

where

$$X (t) = n_{\rm th} (n_{\rm th} - 1) \exp (-2\gamma_m t) + n_{\rm th} (1 - 2n_{\rm th}) \exp (-\gamma_m t) + n_{\rm th}^2. \tag{82}$$

The equations of motion for $\langle c_+^\dagger c_+^\dagger c_+ c_- \rangle$ are found to be

$$\frac{d}{dt}\langle c_+^\dagger c_+^\dagger c_+ c_- \rangle = i2J\langle c_+^\dagger c_+^\dagger c_+ c_- \sigma_z \rangle + 2\gamma_m n_{\rm th}\langle c_+^\dagger c_- \rangle - 2\gamma_m \langle c_+^\dagger c_+^\dagger c_+ c_- \rangle, \tag{83}$$

$$\frac{d}{dt}\langle c_+^\dagger c_+^\dagger c_+ c_- \sigma_z \rangle = i2J\langle c_+^\dagger c_+^\dagger c_+ c_- \sigma_z^2 \rangle + 2\gamma_m n_{\rm th}\langle c_+^\dagger c_- \sigma_z \rangle - 2\gamma_m \langle c_+^\dagger c_+^\dagger c_+ c_- \sigma_z \rangle, \tag{84}$$

$$\frac{d}{dt}\langle c_+^\dagger c_+^\dagger c_+ c_- \sigma_z^2 \rangle = i2J\langle c_+^\dagger c_+^\dagger c_+ c_- \rangle + 2\gamma_m n_{\rm th}\langle c_+^\dagger c_- \sigma_z^2 \rangle - 2\gamma_m \langle c_+^\dagger c_+^\dagger c_+ c_- \sigma_z^2 \rangle. \tag{85}$$

Together with Eq. (64), solving straightforwardly the coupled differential equations (84) and (85) results in

$$\langle c_+^\dagger c_+^\dagger c_+ c_- \sigma_z \rangle (t) = -n_{\rm th}\left[1 - \exp\left(-\gamma_m t\right)\right] \exp\left(-i2Jt\right) \exp\left(-\gamma_m t\right), \tag{86}$$

which, in turn, gives

$$\langle c_+^\dagger c_+^\dagger c_+ c_- \rangle (\tau_0) = -iY(\tau_0), \tag{87}$$

where

$$Y(t) = n_{\rm th}\left[1 - \exp\left(-\gamma_m t\right)\right] \exp\left(-\gamma_m t\right). \tag{88}$$

In a treatment similar to that used for $\langle c_+^\dagger c_+^\dagger c_+ c_- \rangle$, we obtain

$$\langle c_+^\dagger c_-^\dagger c_- c_- \rangle (\tau_0) = -iY(\tau_0), \tag{89}$$

$$\langle c_+^\dagger c_+^\dagger c_- c_- \rangle (\tau_0) = 0. \tag{90}$$

Upon combining Eqs. (80), (81), (87), (89), and (90), this yields, after inversion back to the localized-mode basis,

$$\langle b_k^\dagger b_k^\dagger b_k b_k \rangle (\tau_0) = 2X(\tau_0), \tag{91}$$

$$\langle b_1^\dagger b_1 b_2^\dagger b_2 \rangle (\tau_0) = X(\tau_0), \tag{92}$$

$$\langle b_1^\dagger b_1^\dagger b_1 b_2 \rangle (\tau_0) = \langle b_1^\dagger b_2^\dagger b_2 b_2 \rangle (\tau_0) = iY(\tau_0), \tag{93}$$

$$\langle b_1^\dagger b_1^\dagger b_2 b_2 \rangle (\tau_0) = 0. \tag{94}$$

During the second evolution interval $\tau_0 < t \leq \tau_0 + \tau_1$, the dynamics of the system is driven by the master equation given in Eq. (52), but with $H(t)$ replaced by H_1. Thus, as mentioned in Sec. III, the system has a dynamical evolution similar to what has already been discussed with the delocalized-mode basis in the first interval. We follow the same recipe as above and then find

$$\langle b_k^\dagger b_k^\dagger b_k b_k \rangle (\tau_0 + \tau_1) = 2X(\tau_0 + \tau_1), \tag{95}$$

$$\langle b_1^\dagger b_1 b_2^\dagger b_2 \rangle (\tau_0 + \tau_1) = X(\tau_0 + \tau_1), \tag{96}$$

$$\langle b_1^\dagger b_1^\dagger b_1 b_2 \rangle (\tau_0 + \tau_1) = \langle b_1^\dagger b_2^\dagger b_2 b_2 \rangle (\tau_0 + \tau_1) = i\exp\left(-iJ\tau_1\right) Y(\tau_0 + \tau_1), \tag{97}$$

$$\langle b_1^\dagger b_1^\dagger b_2 b_2 \rangle (\tau_0 + \tau_1) = 0, \tag{98}$$

at the end of this interval.

For the third evolution interval $\tau_0 + \tau_1 < t \leq \tau_T$, we return back to the master equation in Eq. (58), and also back to the delocalized-mode basis. According to Eqs. (95), (96), (97), and (98), the evolution at this stage starts from

$$\langle c_\pm^\dagger c_\pm^\dagger c_\pm c_\pm \rangle (\tau_0 + \tau_1) = 2X(\tau_0 + \tau_1) \mp i2\sin\left(J\tau_1\right) Y(\tau_0 + \tau_1), \tag{99}$$

$$\langle c_+^\dagger c_+ c_-^\dagger c_- \rangle (\tau_0 + \tau_1) = X(\tau_0 + \tau_1), \tag{100}$$

$$\langle c_+^\dagger c_+^\dagger c_+ c_- \rangle (\tau_0 + \tau_1) = \langle c_+^\dagger c_-^\dagger c_- c_- \rangle (\tau_0 + \tau_1) = -i\cos\left(J\tau_1\right) Y(\tau_0 + \tau_1), \tag{101}$$

$$\langle c_+^\dagger c_+^\dagger c_+ c_- \sigma_z^j \rangle (\tau_0 + \tau_1) = \langle c_+^\dagger c_-^\dagger c_- c_- \sigma_z^j \rangle (\tau_0 + \tau_1) = i(-1)^{j+1} \sin^2(\varphi) \cos\left(J\tau_1\right) Y(\tau_0 + \tau_1), \tag{102}$$

$$\langle c_+^\dagger c_+^\dagger c_- c_- \rangle (\tau_0 + \tau_1) = \langle c_+^\dagger c_+^\dagger c_- c_- \sigma_z^j \rangle (\tau_0 + \tau_1) = 0, \tag{103}$$

where $j = 1, 2$. Note that, before this evolution, the spin state has already been transformed from $|D\rangle \to \cos(\varphi)|0\rangle + \sin(\varphi)|D\rangle$ via a single-qubit rotation. Then, by following the same procedure as in the first interval, the last evolution ends with

$$\langle c_{\pm}^{\dagger} c_{\pm}^{\dagger} c_{\pm} c_{\pm} \rangle (\tau_T) = 2X(\tau_T) \pm 2\sin(J\tau_1) Y(\tau_T), \tag{104}$$

$$\langle c_{+}^{\dagger} c_{+} c_{-}^{\dagger} c_{-} \rangle (\tau_T) = X(\tau_T), \tag{105}$$

$$\langle c_{+}^{\dagger} c_{+}^{\dagger} c_{+} c_{-} \rangle (\tau_T) = \langle c_{+}^{\dagger} c_{-}^{\dagger} c_{-} c_{-} \rangle (\tau_T) = -i\cos(J\tau_1) \left[\cos^2(\varphi) - i\sin^2(\varphi)\right] Y(\tau_T), \tag{106}$$

$$\langle c_{+}^{\dagger} c_{+}^{\dagger} c_{-} c_{-} \rangle (\tau_T) = 0, \tag{107}$$

and as a result, with

$$\langle b_k^{\dagger} b_k^{\dagger} b_k b_k \rangle (\tau_T) = 2X(\tau_T) + 2(-1)^j \sin^2(\varphi) \cos(J\tau_1) Y(\tau_T). \tag{108}$$

It is seen that on the right-hand side of Eq. (108), the first term arises from the particle behavior of a phonon and the second term arises from its wave behavior.

By substituting Eq. (108) into Eq. (77), the fluctuation δn_k in the occupation n_k is given by

$$\begin{aligned}(\delta n_k)^2 = &\left(n_{\rm th}^2 - 2P_k n_{\rm th} - P_k^2\right) \exp(-2\gamma_m \tau_T) \\ &- (2n_{\rm th} + 1)(n_{\rm th} - P_k) \exp(-\gamma_m \tau_T) + n_{\rm th}(n_{\rm th} + 1).\end{aligned} \tag{109}$$

Since $\gamma_m \tau_T \ll 1$, we have

$$(\delta n_k)^2 \simeq \left(\delta n_k^{\rm signal}\right)^2 + \left(\delta n_k^{\rm noise}\right)^2, \tag{110}$$

where

$$\left(\delta n_k^{\rm signal}\right)^2 = P_k(1 - P_k), \tag{111}$$

$$\left(\delta n_k^{\rm noise}\right)^2 = P_k(2P_k - 1)\gamma_m \tau_T + n_{\rm th}\gamma_m \tau_T (2P_k + 1). \tag{112}$$

Here, $\delta n_k^{\rm signal}$, the quantum fluctuation induced by the Heisenberg uncertainty principle, accounts for the coherent signal, and $\delta n_k^{\rm noise}$ represents the fluctuation noise, including the vacuum (the first term) and thermal (the second term) fluctuations. To confirm the predictions of Eq. (110), we perform numerics, as shown in Fig. 5. Specifically, we plot the fluctuation noises $\delta n_1^{\rm noise}$ and $\delta n_2^{\rm noise}$ versus the relative phase ϕ. The analytical expression is in excellent agreement with our numerical simulations. Furthermore, the respective CNT signal-to-noise ratios can be defined as

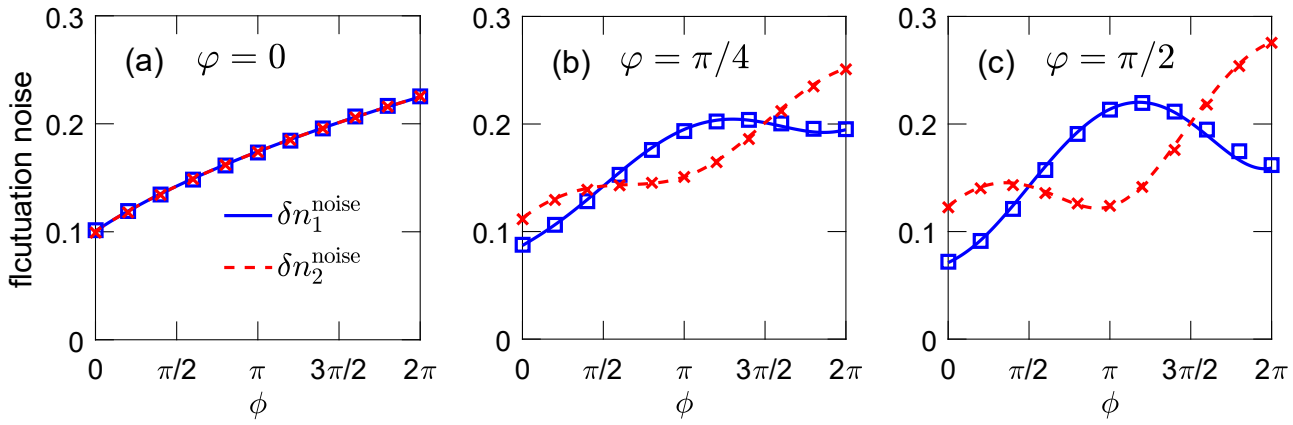

FIG. 5. (Color online) Fluctuation noise $\delta n_1^{\rm noise}$ and $\delta n_2^{\rm noise}$ as a function of the phase ϕ. (a) $\varphi = 0$, (b) $\pi/4$, and (c) $\pi/2$. Solid and dashed curves are analytical results for $\delta n_1^{\rm noise}$ and $\delta n_2^{\rm noise}$, respectively, and symbols correspond to numerical simulations. These analytical and numerical results exhibit an exact agreement. For all plots, in addition to $\gamma_s/2\pi = 200\gamma_m/2\pi = 80$ Hz, we have assumed that $g/2\pi = 100$ kHz, $\omega_m/2\pi = 2$ MHz, $\Omega = 10\omega_m$, and $\Delta_- = 142\omega_m$, resulting in $\omega_q \simeq 1.5\omega_m$ and then $J/2\pi \simeq 12$ kHz. We have also assumed that $n_{\rm th} = 100$, corresponding to an environmental temperature of $\simeq 10$ mK.

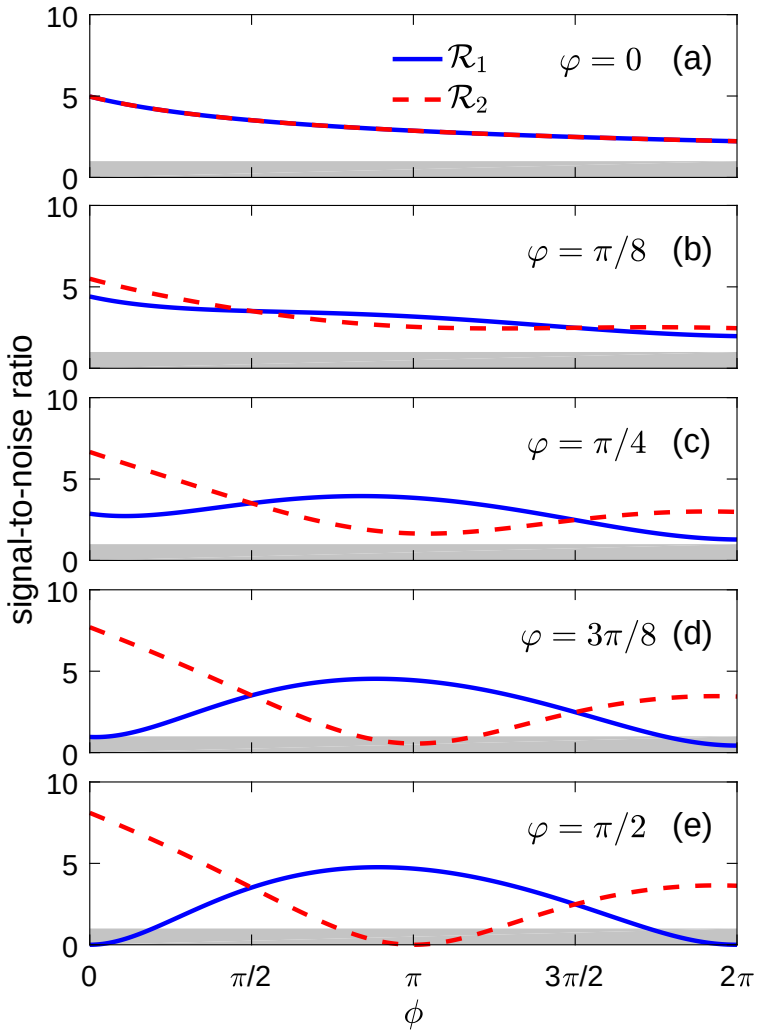

FIG. 6. (Color online) Signal-to-noise ratios $\mathcal{R}_1$ and $\mathcal{R}_2$. (a) $\varphi = 0$, (b) $\pi/8$, (c) $\pi/4$, (d) $3\pi/8$, and (e) $\pi/2$. The solid curves show $\mathcal{R}_1$, while the dashed curves show $\mathcal{R}_2$. The gray shaded area represents the region, where the signal cannot be resolved. For all plots, all other parameters have been set to be the same as in Fig. 5.

$$\mathcal{R}_k = \frac{P_k}{\delta n_k^{\text{noise}}}. \tag{113}$$

Note that, here, we did not use δn_k to define $\mathcal{R}_k$ because $\delta n_k^{\text{signal}}$ in δn_k results from quantum fluctuations of the desired signal, as mentioned previously; and therefore this is not the environmental noise. In order to resolve a signal from the fluctuation noise, the ratio $\mathcal{R}_k$ is required to be $\mathcal{R}_k > 1$. However, Eq. (113) demonstrates that this criterion is not always met for all values of P_k, in particular, at finite temperatures. For example, $P_k = 0$ leads directly to $\mathcal{R}_k = 0$. To address this problem, we now consider the total fluctuation noise,

$$\mathcal{S}^2 = \left(\delta n_1^{\text{noise}}\right)^2 + \left(\delta n_2^{\text{noise}}\right)^2. \tag{114}$$

We further assume that

$$\mathcal{S}^2 < P_1^2 + P_2^2. \tag{115}$$

Under this assumption, if $\mathcal{R}_k < 1$, then $\mathcal{R}_{3-k} > 1$ for $k = 1, 2$; otherwise $\mathcal{R}_1 > 1$, $\mathcal{R}_2 > 1$. This means that at least one of the signals, P_1 or P_2, is resolved for each measurement. Because the coherent phonon number equal to 1 is conserved, and therefore the signals in the two CNTs are complementary, the unresolved signal can be completely deduced from the resolved one. Thus, the criterion in Eq. (115) ensures that the morphing behavior between wave

and particle can be observed from the environment-induced fluctuation noise. In fact, for any value of P_k, the total noise $\mathcal{S}$ is limited by an upper bound,

$$\mathcal{S} < \mathcal{B} \equiv \sqrt{\gamma_m \tau_T^{\max} + 4 n_{\rm th} \gamma_m \tau_T^{\max}}, \tag{116}$$

which is independent of P_k. Meanwhile, $\sqrt{P_1^2 + P_2^2}$ is also limited by a lower bound $\sqrt{2}/2$. Thereby, in order to meet the criterion given in Eq. (115), it is required that

$$\mathcal{B} < \frac{\sqrt{2}}{2}. \tag{117}$$

Based on this condition, we can define a signal visibility

$$\mathcal{R} = \frac{\sqrt{2}}{2\mathcal{B}}, \tag{118}$$

in analogy to R_k. When $\mathcal{R} > 1$, the morphing between wave and particle can be observed, and cannot otherwise. This, in turn, leads to an upper bound on the equilibrium phonon occupation,

$$n_{\rm th} < \frac{1 - 2\gamma_m \tau_T^{\max}}{8 \gamma_m \tau_T^{\max}}, \tag{119}$$

and therefore an upper bound on the temperature,

$$T < \frac{\hbar \omega_m}{k_B \ln\left[\left(1 + 6\gamma_m \tau_T^{\max}\right) / \left(1 - 2\gamma_m \tau_T^{\max}\right)\right]}. \tag{120}$$

Because $\tau_T^{\max} \simeq 5\pi/2J$, the critical temperature is

$$T_{\rm c} = \frac{\hbar \omega_m}{k_B \ln\left[\left(1 + 15\pi\gamma_m/J\right) / \left(1 - 5\pi\gamma_m/J\right)\right]}. \tag{121}$$

In Fig. 6 we plot the signal-to-noise ratios $\mathcal{R}_1$ and $\mathcal{R}_2$ at the temperature $T \simeq 10$ mK. We find that almost all signals can be resolved, and also, as expected, find that when the signal in one CNT is unresolved, the signal in the other CNT is resolved. In fact, the upper bound $\mathcal{B}$ is the fluctuation noise in the total phonon occupation $\langle b_1^\dagger b_1 + b_2^\dagger b_2 \rangle$ at time τ_T. The criterion $\mathcal{R} > 1$ heralds that to resolve the morphing behavior, the fluctuation noise in $\langle b_1^\dagger b_1 + b_2^\dagger b_2 \rangle (\tau_T)$ is required to be smaller than $\sqrt{2}/2$.

V. Numerical simulations

In order to confirm our analytical results, we need to numerically simulate the dynamics with the full master equation given by

$$\begin{aligned} \dot{\rho}(t) =& \frac{i}{\hbar}\left[\rho(t), H_F\right] - \frac{\gamma_s}{2}\mathcal{L}\left(\sigma_z'\right)\rho(t) \\ & - \frac{\gamma_m}{2} n_{\rm th} \sum_{k=1,2} \mathcal{L}\left(b_k^\dagger\right)\rho(t) - \frac{\gamma_m}{2}\left(n_{\rm th}+1\right)\sum_{k=1,2}\mathcal{L}\left(b_k\right)\rho(t), \end{aligned} \tag{122}$$

where $\sigma_z' = |D\rangle\langle D| - |0\rangle\langle 0|$, and H_F is the full Hamiltonian of Eq. (8). Here, we use the Python framework QuTiP [24, 25] to set up this problem. However, the full Hamiltonian is time-dependent, and it takes a long time to integrate the corresponding Schrödinger equation or the master equation, in particular, for our case, where all quantum gates result from the deterministic time evolution of the system. Thus, in our numerical simulations, we replace H_F with $H_{\rm low} + \overline{H}_{\rm high}$, as in Eq. (13). This is a reasonable replacement because in our proposal Ω (tens of MHz) is required to be much smaller than Δ' (up to $\sim$ GHz). In Fig. 7, we plot the unitary evolution of the phonon occupations, $\langle b_1^\dagger b_1 \rangle$ and $\langle b_2^\dagger b_2 \rangle$, of the CNTs. Symbols are the exact results from the full Hamiltonian H_F and solid curves are given by the approximate Hamiltonian $H_{\rm low} + \overline{H}_{\rm high}$. We find an excellent agreement for a very long evolution time, and thus H_F can be very well approximated by $H_{\rm low} + \overline{H}_{\rm high}$. For additional comparison, we also plot the phonon occupation evolution driven only by the low-frequency component $H_{\rm low}$, corresponding to dotted curves. As seen in Fig. 7, owing to the error accumulation, the dynamics of $H_{\rm low}$ deviates largely from the full dynamics of H_F, even within one oscillation cycle. With the above replacement, we obtain the numerical simulations plotted in Fig. 2 of the article, and also in Fig. 5 of the Supplemental Material.

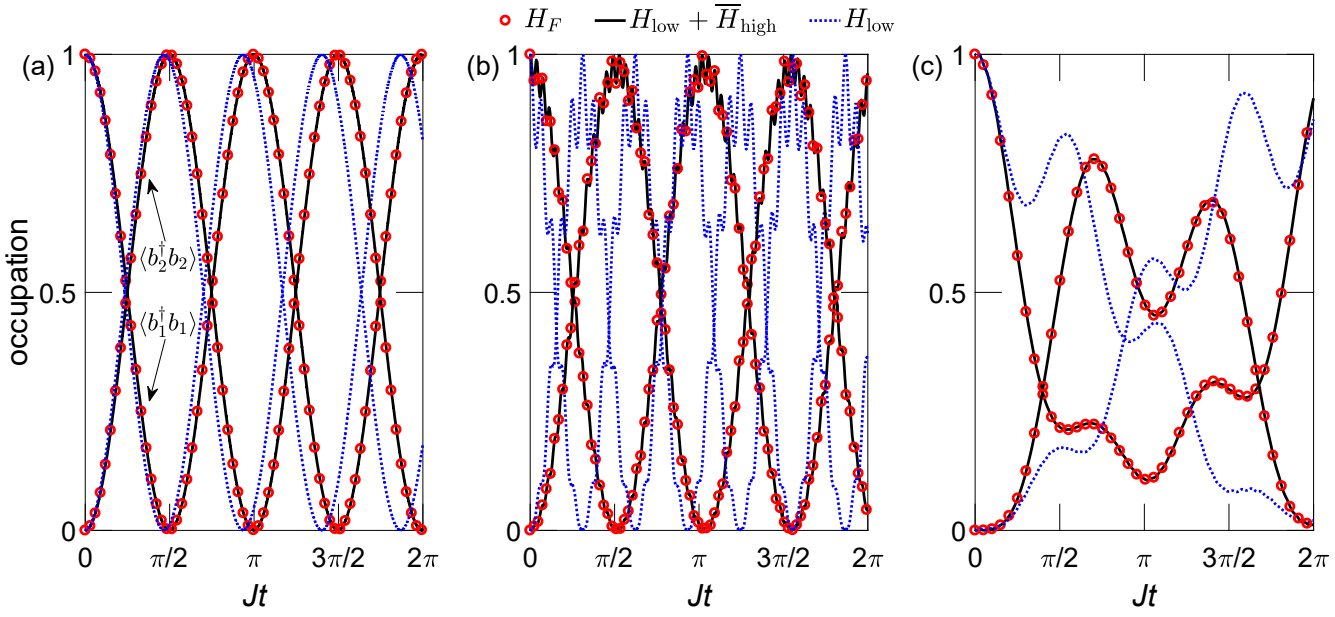

FIG. 7. (Color online) Unitary evolution of the CNT phonon occupations, $\langle b_1^\dagger b_1\rangle$ and $\langle b_2^\dagger b_2\rangle$, for (a) $\Delta_- = 10\Omega$, (b) 25Ω, and (c) 35Ω. The symbols, solid, and dotted curves are obtained, respectively, from H_F, $H_{\rm low}+H_{\rm high}$, and $H_{\rm low}$. For all plots here we have assumed that $\omega_m/2\pi = 2$ MHz, $\Omega = 15\omega_m$, $\omega_0 = D-\Delta_-$, $\Delta_+ = D+\omega_0$, $\Delta = \Delta_- + 3\Omega^2/\Delta_+$, $\omega_q = 2\Omega^2/\Delta + 2\Omega^2/\Delta_+$, and $J = 2\omega_q g^2/\left(\omega_q^2-\omega_m^2\right)$, with a symmetric coupling strength $g/2\pi = 100$ kHz and an initial state $|\Psi\rangle_i = \left(b_1^\dagger\otimes\mathcal{I}_2|{\rm vac}\rangle\right)\otimes|D\rangle$.

[1] Gamel, O. & James, D. F. V. Time-averaged quantum dynamics and the validity of the effective Hamiltonian model. *Phys. Rev. A* **82**, 052106 (2010). URL https://link.aps.org/doi/10.1103/PhysRevA.82.052106.

[2] Qin, W. *et al.* Exponentially Enhanced Light-Matter Interaction, Cooperativities, and Steady-State Entanglement Using Parametric Amplification. *Phys. Rev. Lett.* **120**, 093601 (2018). URL https://link.aps.org/doi/10.1103/PhysRevLett.120.093601.

[3] Sazonova, V. *et al.* A tunable carbon nanotube electromechanical oscillator. *Nature (London)* **431**, 284 (2004). URL http://dx.doi.org/10.1038/nature02905.

[4] Üstünel, H., Roundy, D. & Arias, T. A. Modeling a suspended nanotube oscillator. *Nano Lett.* **5**, 523–526 (2005). URL https://doi.org/10.1021/nl0481371.

[5] Garcia-Sanchez, D. *et al.* Mechanical Detection of Carbon Nanotube Resonator Vibrations. *Phys. Rev. Lett.* **99**, 085501 (2007). URL https://link.aps.org/doi/10.1103/PhysRevLett.99.085501.

[6] Ning, Z. Y. *et al.* Transversally and axially tunable carbon nanotube resonators in situ fabricated and studied inside a scanning electron microscope. *Nano Lett.* **14**, 1221–1227 (2014). URL https://doi.org/10.1021/nl4040913.

[7] Truax, S., Lee, S.-W., Muoth, M. & Hierold, C. Axially tunable carbon nanotube resonators using co-integrated microactuators. *Nano Lett.* **14**, 6092–6096 (2014). URL https://doi.org/10.1021/nl501853w.

[8] Tsioutsios, I., Tavernarakis, A., Osmond, J., Verlot, P. & Bachtold, A. Real-time measurement of nanotube resonator fluctuations in an electron microscope. *Nano Lett.* **17**, 1748–1755 (2017). URL https://doi.org/10.1021/acs.nanolett.6b05065.

[9] Liu, D. E. Sensing kondo correlations in a suspended carbon nanotube mechanical resonator with spin-orbit coupling. *Quantum Engineering* **1**, e10 (2019). URL https://onlinelibrary.wiley.com/doi/full/10.1002/que2.10.

[10] Chaves, R., Lemos, G. B. & Pienaar, J. Causal Modeling the Delayed-Choice Experiment. *Phys. Rev. Lett.* **120**, 190401 (2018). URL https://link.aps.org/doi/10.1103/PhysRevLett.120.190401.

[11] Huang, H.-L. *et al.* A loophole-free Wheeler-delayed-choice experiment. *arXiv preprint arXiv:1806.00156* (2018). URL https://arxiv.org/abs/1806.00156.

[12] Polino, E. *et al.* Device independent certification of a quantum delayed choice experiment. *arXiv preprint arXiv:1806.00211* (2018). URL https://arxiv.org/abs/1806.00211.

[13] Yu, S. *et al.* Experimental realization of causality-assisted Wheeler's delayed-choice experiment using single photons. *arXiv preprint arXiv:1806.03689* (2018). URL https://arxiv.org/abs/1806.03689.

[14] Peruzzo, A., Shadbolt, P., Brunner, N., Popescu, S. & O'Brien, J. L. A Quantum Delayed-Choice Experiment. *Science* **338**, 634–637 (2012). URL http://science.sciencemag.org/content/338/6107/634.

[15] Kaiser, F., Coudreau, T., Milman, P., Ostrowsky, D. B. & Tanzilli, S. Entanglement-Enabled Delayed-Choice Experiment. *Science* **338**, 637–640 (2012). URL http://science.sciencemag.org/content/338/6107/637.

[16] Zheng, S.-B. *et al.* Quantum Delayed-Choice Experiment with a Beam Splitter in a Quantum Superposition. *Phys. Rev. Lett.* **115**, 260403 (2015). URL https://link.aps.org/doi/10.1103/PhysRevLett.115.260403.

[17] Liu, K. *et al.* A twofold quantum delayed-choice experiment in a superconducting circuit. *Sci. Adv.* **3**, e1603159 (2017). URL http://advances.sciencemag.org/content/3/5/e1603159.

[18] Huang, P. *et al.* Observation of an anomalous decoherence effect in a quantum bath at room temperature. *Nat. Commun.* **2**, 570 (2011). URL http://dx.doi.org/10.1038/ncomms1579.

[19] Lillie, S. E. *et al.* Environmentally Mediated Coherent Control of a Spin Qubit in Diamond. *Phys. Rev. Lett.* **118**, 167204 (2017). URL https://link.aps.org/doi/10.1103/PhysRevLett.118.167204.

[20] Xing, J. *et al.* Experimental investigation of quantum entropic uncertainty relations for multiple measurements in pure diamond. *Sci. Rep.* **7**, 2563 (2017). URL https://doi.org/10.1038/s41598-017-02424-6.

[21] Balasubramanian, G. *et al.* Ultralong spin coherence time in isotopically engineered diamond. *Nat. Mater.* **8**, 383–387 (2009). URL http://dx.doi.org/10.1038/nmat2420.

[22] Bar-Gill, N., Pham, L. M., Jarmola, A., Budker, D. & Walsworth, R. L. Solid-state electronic spin coherence time approaching one second. *Nat. Commun.* **4**, 1743 (2013). URL http://dx.doi.org/10.1038/ncomms2771.

[23] Moser, J., Eichler, A., Güttinger, J., Dykman, M. I. & Bachtold, A. Nanotube mechanical resonators with quality factors of up to 5 million. *Nat. Nanotechnol.* **9**, 1007–1011 (2014). URL http://dx.doi.org/10.1038/nnano.2014.234.

[24] Johansson, J. R., Nation, P. D. & Nori, F. Qutip: An open-source Python framework for the dynamics of open quantum systems. *Comput. Phys. Commun.* **183**, 1760–1772 (2012). URL http://www.sciencedirect.com/science/article/pii/S0010465512000835.

[25] Johansson, J. R., Nation, P. D. & Nori, F. Qutip 2: A Python framework for the dynamics of open quantum systems. *Comput. Phys. Commun.* **184**, 1234–1240 (2013). URL http://www.sciencedirect.com/science/article/pii/S0010465512003955.